scientific reports

Check for updates

OPEN

Graphene metasurfaces biosensor for COVID-19 detection in the infra-red regime

Hussein A. Elsayed[1], Jacob Wekalao[2]✉, Ahmed Mehaney[3], Haifa E. Alfassam[4], Mostafa R. Abukhadra[5,6], Ali Hajjiah[7] & Wail Al Zoubi[8]

This study presents the design and analysis of a biosensor for COVID-19 detection, integrating graphene metasurfaces with gold, silver, and GST materials. The proposed sensor architecture combines a square ring resonator with a circular ring resonator, optimized through COMSOL Multiphysics simulations in the infrared regime. The sensor demonstrates exceptional performance characteristics, with absorption values exceeding 99.5% in the primary detection band (4.2–4.6 μm) and approximately 97.5% in the secondary band (5.0–5.5 μm). The device exhibits high sensitivity (4000 nm/RIU), a detection limit of 0.078, and a figure of merit of 16.000 RIU^{-1} when utilizing crystalline GST as the substrate material. The sensor's performance was further enhanced through machine learning optimization using XGBoost regression, achieving perfect correlation (R^2 = 100%) between predicted and experimental values across various operational parameters. The dual-band detection mechanism, combined with the integration of advanced materials and machine learning optimization, offers a promising platform for rapid, label-free, and highly sensitive COVID-19 detection. This research contributes to the development of next-generation biosensing technologies for viral detection and disease diagnosis.

Keywords COVID-19 biosensor, Graphene metasurfaces, Phase change materials, Machine learning optimization, Dual-Band detection, Label-free sensing

The rapid and accurate detection of infectious diseases remains a critical global challenge, particularly in the wake of pandemics such as COVID-19[1]. Early and precise diagnosis plays a crucial role in mitigating transmission and guiding effective treatment strategies[2]. Conventional diagnostic methods, including polymerase chain reaction (PCR) and antigen-based tests, while highly specific, often suffer from limitations such as long processing times, high costs, and the need for specialized laboratory environments[3]. These challenges points out the necessity for alternative biosensing platforms that offer real-time, label-free, and highly sensitive detection capabilities.

Metasurfaces-based biosensors have emerged as a promising solution, leveraging engineered nanostructures to manipulate light-matter interactions for enhanced sensitivity and selectivity[4]. Graphene-integrated metasurfaces, in particular, provide tunable electronic and plasmonic properties, making them highly suitable for biomolecular detection[5]. By combining graphene with noble metals such as gold and silver, strong plasmonic resonance effects can be induced, significantly enhancing absorption efficiency and field confinement[6,7]. Furthermore, the incorporation of phase-change materials like GST introduces dynamic tunability, allowing for adaptable sensing platforms capable of real-time resonance tuning[8].

Advancements in materials engineering have extended beyond graphene to include other 2D materials like MXenes and transition metal dichalcogenides (TMDs), which offer unique properties such as high conductivity, chemical versatility, and tunable electronic features for applications in sensing, energy, and catalysis[9–11]. Hybrid nanocomposites, combining materials like graphene with MXenes or TMDs, exploit synergistic effects to enhance mechanical strength, conductivity, and stability, enabling multifunctional applications[12]. Surface

[1]Department of Physics, College of Science, University of Ha'il, P.O. Box, 2440, Ha'il, Saudi Arabia. [2]Department of Optics and Optical Engineering, University of Science and Technology of China, Hefei 230026, China. [3]Physics Department, Faculty of Science, Beni-Suef University, Beni-Suef 62512, Egypt. [4]Department of Biology, college of Science, Princess Nourah bint Abdulrahman University, P.O. BOX 84428, Riyadh 11671, Saudi Arabia. [5]Materials Technologies and their applications Lab, Faculty of Science, Beni-Suef University, Beni Suef City, Egypt. [6]Applied Science Research Center, Applied Science Private University, Al-Jandaweel, Amman 11931, Jordan. [7]Department of Electrical Engineering, College of Engineering and Petroleum, Kuwait University, Kuwait, Kuwait. [8]Materials Electrochemistry Laboratory, School of Materials Science and Engineering, Yeungnam University, Gyeongsan 38541, Republic of Korea. ✉email: jacob1902@mail.ustc.edu.cn

functionalization strategies, including covalent bonding and nanoparticle conjugation, further improve bio-recognition and selectivity, critical for biosensors and diagnostics[13]. Additionally, novel coating materials, such as polymers and metal oxides, enhance stability, reduce fouling, and enable stimuli-responsive functionalities, driving innovations in energy, filtration, and biomedical technologies[14].

In the field of biosensors, significant advancements in techniques and materials have garnered substantial research interest. A detailed numerical analysis of a photonic crystal fibre (PCF)-based plasmonic sensor, integrating silica and 50 nm gold layers, reveals enhanced sensitivity values of -422 RIU^{-1} (amplitude) and 10,000 nm/RIU (wavelength) through finite element method (FEM) simulations. This sensor achieves a high resolution of 1×10^{-5} RIU and operates effectively within the refractive index range of 1.35 to 1.39 RIU[15]. The designed SPR-PCF sensor exhibits exceptional performance with a wavelength sensitivity of 27,000 nm/RIU and amplitude sensitivity of 2944.94 RIU^{-1}, achieving a high resolution of 3.70×10^{-6} RIU and FOM of 692 RIU^{-1} over the RI range 1.34–1.44[16].The novel X-shaped SPR-PCF biosensor delivers outstanding performance with a wavelength sensitivity of 29,000 nm/RIU and amplitude sensitivity of 1581 RIU^{-1}, while achieving high resolution (1.72×10^{-6} RIU) and FOM (558) across the RI range of 1.25–1.42[17].The innovative LRSPR sensor, built with a Cytop/Al 1D photonic crystal design, demonstrates exceptional performance with a peak sensitivity of 5846 RIU^{-1} and detection limit of 5×10^{-7} RIU within 1.328–1.334 RI range, performing 100 times better than traditional SPR sensors[18].A comparative analysis of dual-gist PCF biosensors reveals the gold-coated design outperforms its silver counterpart, achieving higher sensitivity (115,999 nm/RIU vs. 49,000 nm/RIU) and better resolution (8.66×10^{-7} vs. 1.86×10^{-6} RIU), with both sensors operating effectively in the 1.29–1.39 RIU range[19].The MoS_2 based SPR sensor demonstrates dual-sensing capabilities with high refractive index sensitivity (25,800 nm/RIU) in the 1.415–1.420 RI range and excellent temperature response (9.81 nm/°C) from 0 to 100 °C, operating effectively in the NIR region[20]. The innovative bimetallic SPR biosensor, incorporating an optimized $BaTiO_3$ dielectric layer, demonstrates superior performance with 220°/RIU sensitivity for blood plasma analysis[21].

Recent research in COVID-19 detection has emphasized the need for improved testing methods that are quick, dependable, and affordable. While current tests like PCR and antigen testing are accurate, they face several drawbacks including time delays, procedural complexity, and significant expense[22–24]. Therefore, many scholars directed towards some new sensor technologies to address these limitations by combining advanced materials with sophisticated modelling tools. Rajeev et al.[25]demonstrated an SPR sensor for COVID-19 detection, achieving maximum wavelength sensitivities of 5350.87 nm/RIU (RNA), 5333.33 nm/RIU (spike RBD), and 4700.85 nm/RIU (IgG), with limits of detection as low as 1.86×10^{-6} RIU and a penetration depth of 218.07 nm. Mani et al.[26] presented a PCF-based biosensor for SARS-CoV-2 S1-RBD detection, achieving a high sensitivity of 17,282 nm/RIU with a binding affinity of 2.6 kcal/mol, demonstrating efficiency and adaptability for COVID-19 diagnostics.

A promising approach involves metasurfaces - engineered materials with microscopic structures that can control electromagnetic waves in unique ways. These biosensors incorporate various materials including graphene, gold, silver, and black phosphorus, each offering specific advantages. The combination allows for highly sensitive detection without requiring additional labels, and can identify viral markers even in small amounts.

Therefore, we have introduced in this study a graphene metasurfaces-based biosensor that integrates gold, silver, and black phosphorus for the detection of COVID-19 biomarkers. Using COMSOL Multiphysics version 6.2, we modelled and simulated the sensor's performance in the infrared regime, where the sensor's resonance properties can be leveraged for high-precision detection. The combination of these advanced materials and the powerful simulation environment enables the design of a highly sensitive and rapid diagnostic tool that could be capable of detecting the virus in real-time, potentially revolutionizing early-stage detection and monitoring of COVID-19. Each material serves a distinct purpose: graphene provides excellent electrical properties and surface area for biological interactions, gold and silver create strong SPR that improve sensitivity to refractive index changes, and black phosphorus contributes valuable optoelectronic properties that enhance viral detection.

Theoretical framework

Design methodology

Figure 1 presents the architecture of the proposed biosensor design, which features precisely calibrated resonator and layer thicknesses to optimize performance. At its core, the device incorporates a square ring (SR) resonator with inner and outer dimensions of 3.5 µm and 4.5 µm, respectively. This central SR structure is surrounded by a circular ring (CR) resonator with dimensions of 3.5 µm and 4 µm. Both resonator structures are positioned at the centre of a 9 µm square base to ensure optimal interaction with incident light. The resonator components, both SR and CR, maintain a uniform thickness of 1 µm to maximize resonance and minimize scattering losses. The underlying substrate layer, composed of aGST and Cgst which are varied alternatively, measures 1.6 µm in thickness, providing mechanical support and minimizing unwanted parasitic effects. The overall substrate platform spans 10 µm in both length and width, creating a compact, efficient sensing surface. Detailed visualizations of the design are provided in Fig. 1, which displays the structure from top-down (panel a), three-dimensional (panel b), and side perspectives (panel c), offering a comprehensive view of the sensor's layout and geometry.

Table 1 demonstrates the initial parameters of the proposed sensor design.

The simulations employ Wave Optics Module of **COMSOL version 6.2**[27–29] that is essentially based on the basics of the finite element method (FEM). Meanwhile, the computational domain is designed with perfectly matched layers (PMLs) on all outer boundaries to prevent artificial reflections and ensure accurate electromagnetic wave propagation. In addition, the meshing strategy involves an adaptive mesh

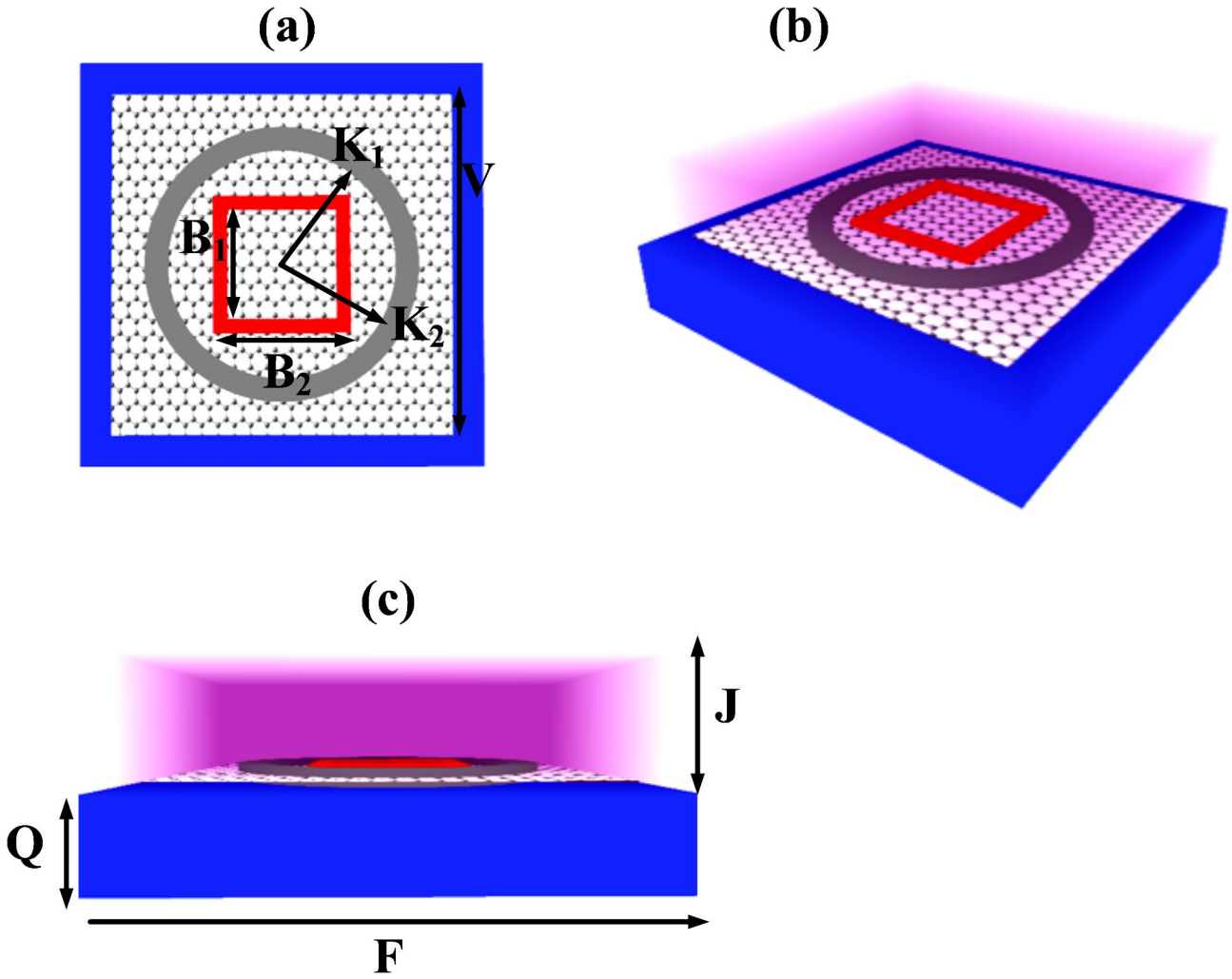

Fig. 1. Presents three different views of the sensor's construction: a top-down view (**a**), a three-dimensional representation (**b**), and a cross-section from the front (**c**).

Parameter	B_1	B_2	K_1	K_2	V	F	Q	J
Size (μm)	3.5	4.5	3.5	4	9	10	1.6	1.69

Table 1. The numerical specifications of the Sensor's design components.

refinement approach, where the maximum element size is set to 0.833 nm near the resonator structures to resolve fine geometrical features and field variations, while a coarser mesh is applied in less critical regions to optimize computational efficiency. The solver settings include the use of a frequency-domain solver with a relative tolerance of 10^{-6} to ensure convergence, and an iterative solver configuration with an appropriate preconditioner to handle large-scale matrix computations effectively.

The material composition is represented through a color-coded scheme, where silver components are shown in red, Gold elements are depicted in purple, and GST (a and c) regions are represented in blue. Notably, the square resonator is coated with a layer of graphene, chosen for its remarkable electronic and optical properties. The graphene layer enhances the sensor's sensitivity to changes in the refractive index of surrounding media, making it highly suitable for biosensing applications. To evaluate the sensor's performance, we conducted electromagnetic simulations using COMSOL Multiphysics' finite element method (FEM) framework. The analysis utilized the wave optics module's electromagnetic waves wavelength domain interface to model the light interaction with the metasurfaces. The mesh configuration was carefully customized with elements ranging from 0.833 nm (maximum) to 0.5 nm (minimum), ensuring high accuracy in capturing the intricate light propagation and resonance effects within the structure. The design also includes input and output ports for light transmission and termination, facilitating the interaction with external optical systems for sensor signal detection. Incorporating and cGST into the sensor design offers an interesting approach by utilizing two different types of graphene

oxide derivatives for enhancing sensitivity. The use of aGST and cGST can potentially improve the sensor's performance by providing distinct surface properties that enhance the interaction between the sensor and target biomolecules. This results to more precise detection, as each variant may have unique affinity or binding characteristics for specific analytes, such as viral particles in the case of COVID-19 detection. Additionally, the combination of these two materials helps in fine-tuning the sensor's response, broadening its application range, and improving the overall sensitivity, selectivity, and stability.

Graphene conductivity

The electrical conductivity of graphene is influenced by several variables, such as the introduction of dopants, changes in temperature, and structural imperfections[30]. When graphene is doped with materials that either donate or accept electrons, this alters the concentration of charge carriers, thereby changing its conductivity. The number of graphene layers also plays a crucial role - single-layer graphene demonstrates superior conductivity since additional layers can create scatter effects that diminish electron mobility[31]. Graphene's remarkable combination of properties - excellent electrical conductivity, robust mechanical characteristics, flexibility, and optical transparency - positions it as an attractive candidate for numerous technological applications, from cutting-edge electronics and sensing devices to energy storage solutions and transparent conductors[32].The graphene's conductivity (σs) can is calculated using Eq. 1 through 3[33]

$$\epsilon\ (\omega) = 1 + \frac{\sigma_s}{\epsilon_0 \omega \nabla} \tag{1}$$

$$\sigma_{intra} = \frac{-je^2 k_B T}{\pi \hbar^2 (\omega - j2\Gamma)} \left(\frac{\mu_c}{k_B T} + 2 \ln \left(e^{\frac{\mu_c}{k_B T}} + 1 \right) \right) \tag{2}$$

$$\sigma_{inetr} = \frac{-je^2}{4\pi \hbar} \ln \left(\frac{2|\mu_c| - (\omega - j2\Gamma)\hbar}{2|\mu_c| + (\omega - j2\Gamma)\hbar} \right) \tag{3}$$

$$\mu_c = E_f \approx \hbar v_f = \sqrt{\frac{\pi \epsilon_0 \epsilon_{0x} V_g}{e d_{ox}}} \tag{4}$$

Fabrication feasibility

Synthesis of the proposed infrared biosensor architecture necessitates implementation of high-precision nanofabrication methodologies encompassing multiple sequential processes: substrate preparation, material deposition, lithographic patterning, and plasma etching, all executed with nanometric precision. The fabrication protocol initiates with the selection of an appropriate substrate, predominantly GST, which undergoes rigorous solvent-based purification to eliminate surface contaminants, followed by thermal desorption to achieve optimal surface characteristics. Substrate dimensionality is regulated to maintain a uniform thickness of 1.6 µm via precision mechanical processing or anisotropic etching protocols. The material deposition phase represents a critical determinant of device performance. Monolithic graphene films are synthesized via chemical vapor deposition (CVD) methodology and subsequently transferred utilizing a solution-phase protocol. Noble metal (Ag) thin films are deposited in predetermined geometries using physical vapor deposition (PVD) techniques, specifically magnetron sputtering or electron-beam evaporation. The phase-change chalcogenide materials (aGST and cGST) are deposited through atomic layer deposition (ALD) or magnetron sputtering to achieve precisely controlled stoichiometry and layer uniformity. The geometric patterning of the resonator structures (square ring SR and circular ring CR) employs photolithographic techniques. A photosensitive resist is deposited via spin coating, followed by mask-based pattern transfer. For sub-micron feature definition, electron beam lithography (EBL) is implemented, enabling the fabrication of resonator structures with critical dimensions of 3.5 µm and 4.5 µm respectively. Post-lithographic pattern transfer is achieved through reactive ion etching (RIE), with precise control of the plasma chemistry and etch parameters to maintain vertical sidewalls and achieve the specified resonator thickness of 1 µm. The integration of multilayer materials, particularly the phase-change chalcogenide heterostructures, demands stringent contamination control and interface engineering protocols. Post-fabrication thermal treatment protocols may be implemented to optimize interfacial characteristics and enhance mechanical stability. The integration of optical waveguides necessitates submicron alignment precision to achieve optimal coupling efficiency at the input and output ports. Figure 2a–e demonstrates the Fabrication feasibility of the proposed sensor design.

Sensor performing parameters and analyte properties

The device's sensing capabilities can be evaluated by measuring some of its performing parameters such as its sensitivity (S), figure of merit (FOM), quality factor (Q), detection limit (DL), sensor resolution (SR) and detection accuracy (DA). In this regard, these parameters can briefly described as follows:

$$\mathrm{S} = \frac{\Delta \lambda}{\Delta n} \tag{5}$$

$$\mathrm{FOM} = \frac{S}{FWHM} \tag{6}$$

$$\mathrm{Q} = \frac{\lambda r}{FWHM} \tag{7}$$

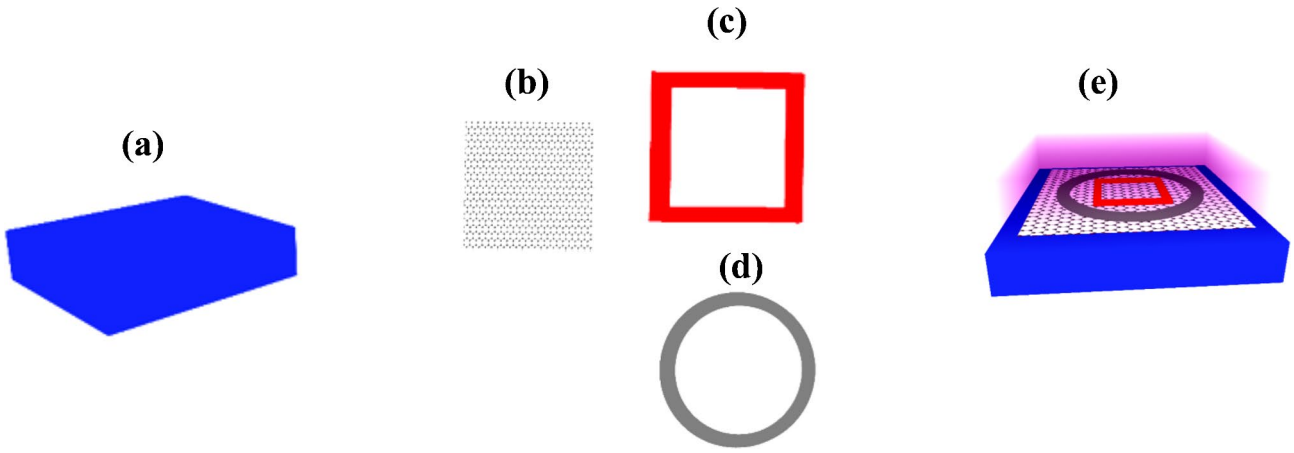

Fig. 2. Fabrication feasibility of the proposed sensor design.

$$\mathrm{DL} = \left(\frac{\Delta n}{1.5}\right) \times \left(\frac{FWHM}{\Delta \lambda}\right)^{1.25} \tag{8}$$

$$\mathrm{DR} = \frac{\lambda_r}{\sqrt{FWHM}} \tag{9}$$

$$\mathrm{SNR} = \frac{\Delta \lambda}{FWHM} \tag{10}$$

$$\mathrm{SR} = S \times DL \tag{11}$$

$$\mathrm{DA} = \frac{1}{FWHM} \tag{12}$$

$$\mathrm{X} = \frac{2(\Delta \lambda)^{0.75}(FWHM)^{0.25}}{9} \tag{13}$$

These equations define essential metrics for evaluating sensor performance. The parameters define various performance metrics for a sensor: Sensitivity (S) measures the change in resonance wavelength per unit change in refractive index; Figure of Merit (FOM) evaluates sensor performance by comparing sensitivity to the resolution (FWHM); Quality Factor (Q) reflects the sharpness of the resonance peak; Detection Limit (DL) determines the smallest detectable refractive index change; Dynamic Range (DR) indicates the range of detectable signals; Signal-to-Noise Ratio (SNR) measures signal quality; Sensor Resolution (SR) combines sensitivity and detection limit to assess overall resolution; Detection Accuracy (DA) quantifies the precision of the sensor, inversely related to FWHM; and Uncertainty (X) gauges the sensor's uncertainty, based on both wavelength change and FWHM. The process of modelling how sensors respond typically requires finding solutions to Maxwell's equations while accounting for specific boundary conditions.

$$\nabla \times \mathrm{E} = \frac{-\partial \mathrm{B}}{\partial \mathrm{t}} \tag{14}$$

$$\nabla \times \mathrm{H} = \mathrm{J} + \frac{\partial \mathrm{D}}{\partial \mathrm{t}} = \tag{15}$$

$$\nabla \cdot \mathrm{D} = \rho \tag{16}$$

$$\nabla \cdot \mathrm{B} = 0 \tag{17}$$

The refractive index-based detection of COVID-19 works by measuring changes in the optical properties of a medium when virus particles or their associated biomarkers are present. When viral antigens or antibodies bind to specifically-designed receptor sites on a sensor's surface (like those using surface plasmon resonance or similar techniques), they create measurable shifts in the local refractive index. This principle enables highly sensitive virus detection systems that can identify even small amounts of viral material through these optical changes.

Table 2 demonstrates different Variants of the COVID-19 Virus. The dual-resonator configuration plays a critical role in sensor performance. The square ring resonator generates high field confinement, while the circular ring resonator extends the plasmonic response across a broader spectral range. Their interplay enables effective mode coupling, where the overlapping resonance modes lead to constructive interference and increased electric field enhancement. This coupling mechanism improves light-matter interactions, leading to superior detection

WHO Label	Pango Lineage	GISAID Clade	Nextstrain Clade	Additional amino acid changes monitored	Earliest documented samples	Date of designation
Alpha	B.1.1.7	GRY	20I (V1)	+S:484 K +S:452R	United Kingdom, Sep 2020	Dec 18, 2020
Beta	B.1.351	GH/501Y.V2	20 H (V2)	+S: L18F	South Africa, May 2020	Dec 18, 2020
Gamma	P.1	GR/501Y.V3	20 J (V3)	+S:681 H	Brazil, Nov 2020	Jan 11, 2021
Delta	B.1.617.2	G/478K.V1	21 A, 21I, 21 J	+S:417 N +S:484 K	India, Oct 2021	VOI: Apr 4, 2021 VOC: May 11, 2021
Lambda	C.37	GR/452Q.V1	21G	–	Peru, Dec 2020	Jun 14, 2021
Mu	B.1.621	GH	21 H	–	Colombia, Jan 2021	Aug 30, 2021
Omicron	B.1.1.529	GRA	21 K, 21 L, 21 M	+R346K	Multiple countries, Nov 2021	VUM: Nov 24, 2021 VOC: Nov 26, 2021

Table 2. Variants of the COVID-19 virus[34].

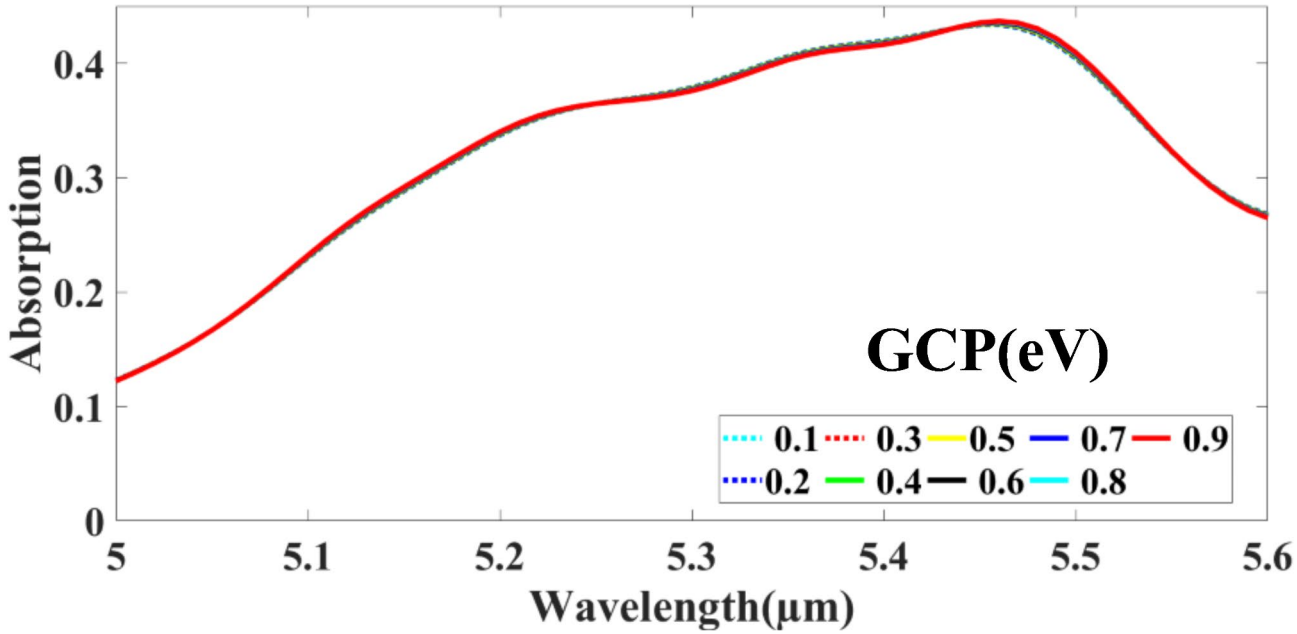

Fig. 3. Absorption response for the variation of Graphene chemical potential.

capabilities. The broadening of resonance peaks due to these effects ensures that the sensor maintains high sensitivity over a wider refractive index range, making it more effective for real-world biosensing applications.

Results and discussion

The analysis in this section focuses on characterizing the proposed biosensor platform through detailed COMSOL Multiphysics simulations. The device architecture, depicted in Fig. 1, was modelled with periodic boundary conditions applied along its lateral dimensions to accurately represent an extended array structure. We conducted extensive parametric studies to evaluate the sensor's response to varying concentrations of SARS-CoV-2 viral particles, examining how changes in the surrounding medium's refractive index influence the detection sensitivity. The investigation explores multiple geometric configurations, including variations in Graphene chemical potential and the angle of incidence. These structural parameters were adjusted to optimize the device's sensing capabilities. The analysis encompasses both near-field electromagnetic distributions and far-field optical responses. In the latter portion of this section, we introduce an advanced machine learning framework developed to enhance the sensor's diagnostic capabilities. This computational approach processes the optical response data to improve detection accuracy and reduce false positives. Through rigorous testing and validation, we identified the optimal configuration that achieved maximum sensitivity for COVID-19 detection, with specific performance metrics detailed in subsequent subsections.

In Fig. 3, the line plot illustrates the variation in graphene chemical potential (GCP) across a 5 **μm** -5.6 **μm** wavelength range. The GCP is varied from 0.1 eV to 0.9 eV in increments of 0.1 eV to analyse its impact on absorption characteristics. The plot highlights the absorption response in the infra red regime, within the wavelength range of 5 μm to 5.6 μm, as the chemical potential increases, with absorption values gradually rising. The s absorption percentages corresponding to GCP values of 0.1 eV to 0.9 eV are as follows: 43.369%, 43.409%,

43.449%, 43.489%, 43.529%, 43.569%, 43.610%, 43.650%, and 43.691%. These results indicate a linear trend of absorption enhancement as GCP increases, demonstrating the tunable nature of graphene's optical properties.

Figure 4 presents the numerical simulation results of the sensor, highlighting that its theoretical performance in the mid-infrared region surpasses that of other spectral regions. This is attributed to the enhanced plasmonic resonance and absorption characteristics within this wavelength range, leading to improved sensitivity and detection efficiency. The enhanced absorption efficiency and plasmonic resonance in the mid-infrared regime contribute to higher sensitivity and improved specificity for biomolecular detection. In the angular dependence study, measurements were conducted across the mid-infrared wavelength range of 4.8–5.4 μm, with incident angles varying from 0° to 80° in precise 10° increments. The absorption characteristics demonstrated exceptional performance and remarkable stability at shallow to moderate angles. The device achieved near-perfect absorption

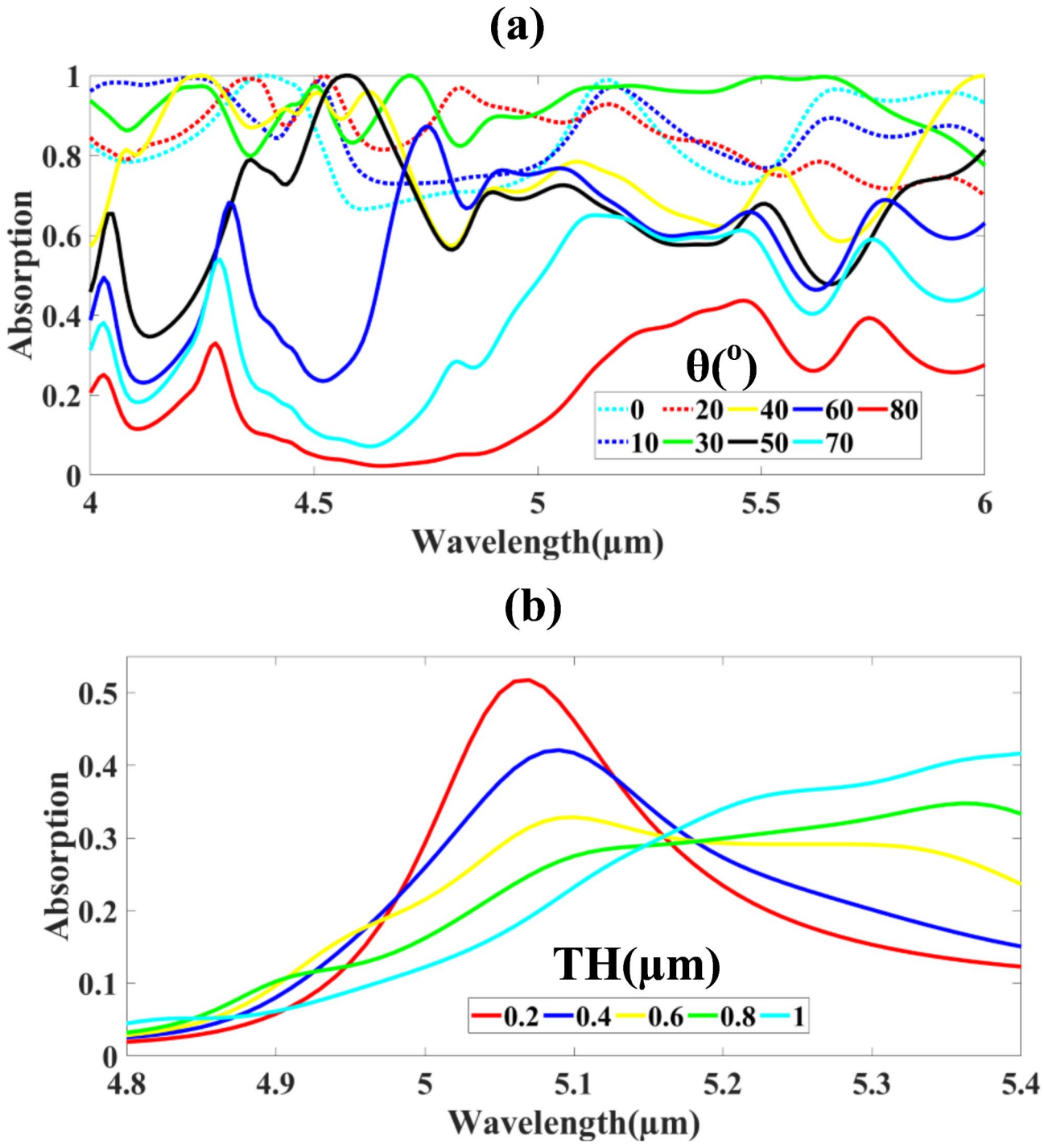

Fig. 4. Absorption response as a function of (**a**) the angle of incidence and (**b**) the thickness variation of circular (CR) and square (SR) resonators.

with values of 99.972% at normal incidence (0°), maintaining this outstanding performance through successive angles: 99.428% at 10°, 99.965% at 20°, 99.939% at 30°, 99.956% at 40°, and 99.977% at 50°. However, a significant performance degradation was observed as the angle of incidence approached more oblique angles. The absorption efficiency exhibited a sharp decline, dropping to 87.242% at 60°, further deteriorating to 65.057% at 70°, and reaching its lowest value of 43.691% at the most extreme angle of 80°. This angular dependency suggests optimal operational conditions at angles below 50°, where the absorption consistently remains above 99%. The second parametric investigation, illustrated in Fig. 4b, focused on the thickness optimization of both the circular (CR) and square (SR) resonators. The analysis explored thickness variations from 0.2 μm to 1.0 μm, implemented in regular 0.2 μm steps. Throughout the same wavelength range (4.8–5.4 μm), the absorption characteristics revealed a more moderate performance profile compared to the angle variation study. The thinnest configuration at 0.2 μm exhibited the highest absorption at 51.756%, followed by a slight decrease to 42.108% at 0.4 μm. As the thickness increased further, the absorption showed minimal variation: 43.982% at 0.6 μm, a slight improvement to 44.943% at 0.8 μm, and finally settling at 43.691% for the maximum thickness of 1.0 μm. This pattern suggests that increasing resonator thickness beyond 0.2 μm does not significantly enhance the absorption characteristics, indicating that thinner resonator structures are preferable from both a performance and material efficiency standpoint.

Figure 5 presents comparative absorption characteristics for two distinct resonator configurations: (a) a circular ring resonator (CR) and (b) a square resonator (SR). For the circular ring resonator analysis (Fig. 5a), the radius was varied from 3.5 μm to 4.5 μm with incremental steps of 0.2 μm. The absorption behaviour was studied in the wavelength range of 4.8 μm to 5.6 μm. The measured absorption values demonstrate variations with changes in resonator dimensions. Starting at 3.5 μm, an absorption of 38.946% was observed, which slightly decreased to 37.814% at 3.7 μm. As the dimensions increased further, the absorption showed an upward trend, reaching 42.002% at 3.9 μm and 42.575% at 4.1 μm. The peak absorption of 44.945% was achieved at 4.3 μm, after which it declined to 39.892% at 4.5 μm. This pattern suggests optimal resonance conditions at the 4.3 μm dimension. For the square resonator configuration (Fig. 5b), the side length was varied from 2.5 μm to 4.5 μm in larger increments of 0.5 μm. The absorption characteristics were analyzed in a slightly different wavelength range of 5.6 μm to 6.0 μm. The absorption measurements showed a distinct pattern: beginning with 65.982% at 2.5 μm, the absorption increased to its maximum value of 69.074% at 3.0 μm. Beyond this point, a consistent decrease was observed, with values of 48.591% at 3.5 μm, 46.990% at 4.0 μm, and finally 43.691% at 4.5 μm. This trend clearly indicates an optimization point for absorption efficiency at the 3.0 μm dimension.

Detection analysis

After optimizing the sensor structure, its performance for COVID-19 detection is evaluated. The analysis demonstrates characteristics in the transmission spectrum, as shown in Fig. 6a-b, where two distinct transmittance drops are observed. Both regions exhibits shifts in absorption response corresponding to variations in refractive indices caused by different COVID-19 concentrations. In the first wavelength band, spanning 4.2 μm to 4.6 μm, the sensor demonstrates exceptionally high absorption characteristics. The absorption values showed a subtle decreasing trend with increasing COVID-19 concentration: starting at 99.535%, then gradually decreasing to 99.526%, 99.518%, 99.515%, and finally reaching 99.503%. This high-sensitivity region maintains absorption values consistently above 99.5%, indicating excellent detection capabilities. The second wavelength band, ranging from 5.0 μm to 5.5 μm, also exhibits remarkable absorption characteristics, albeit slightly lower than the first band. In this region, an inverse trend is observed, with absorption values showing a gradual increase: beginning at 97.557%, then progressively rising to 97.573%, 97.580%, 97.587%, and reaching 97.594%. This consistent upward trend in absorption values suggests a different mechanism of interaction between the sensor and the COVID-19 samples in this wavelength range. The presence of two distinct absorption bands, each showing opposite trends with concentration changes, provides a unique dual-verification capability for COVID-19 detection. The first band's extremely high absorption values (>99.5%) coupled with the second band's complementary behavior (around 97.5%) creates a robust detection mechanism that reduce false positives and increase reliability in COVID-19 sensing applications.

We also evaluated the detection performance of the sensor utilizing cGST as the substrate material. The results of this analysis are depicted in Fig. 7. The plots in Fig. 7(a) and 7(b) illustrate the sensor's transmittance response under varying concentrations of the target analyte, simulating changes in refractive indices due to different COVID-19 concentration levels. Two significant transmittance drops are observed, corresponding to distinct wavelength bands where the absorption response demonstrates sensitivity to refractive index variations. In the first band, spanning 4.15 μm to 4.6 μm, the absorption values obtained are 99.972%, 99.972%, 99.973%, 99.960%, and 99.975%, indicating highly consistent absorption behaviour near total absorption for most concentration levels. In the second band, covering the range from 4.8 μm to 5.5 μm, the absorption values are slightly lower but still significant, recorded as 98.935%, 98.884%, 98.886%, 98.887%, and 98.888%. These results suggest strong sensor performance and a high degree of sensitivity in response to changes in refractive index caused by varying COVID-19 concentrations. Figure 7 highlights the potential of GST as an effective substrate material for biosensing applications due to its unique phase-change properties. The ability of GST to switch between amorphous and crystalline states enables dynamic modulation of its optical properties, allowing for tunable absorption characteristics across multiple wavelength bands. This tunability enhances the sensor's detection precision by providing distinct resonance conditions for different analytes, improving selectivity and minimizing false positives. Additionally, GST's high refractive index contrast supports strong electromagnetic field confinement, which boosts sensitivity and ensures accurate biomolecular detection. Graphene, gold, and silver collectively contribute to the enhancement of plasmonic resonance, with each material serving a specific role. Graphene's tunable conductivity enables active modulation of surface plasmon polaritons, improving sensitivity. Silver enhances field confinement due to its superior plasmonic properties, while gold provides long-

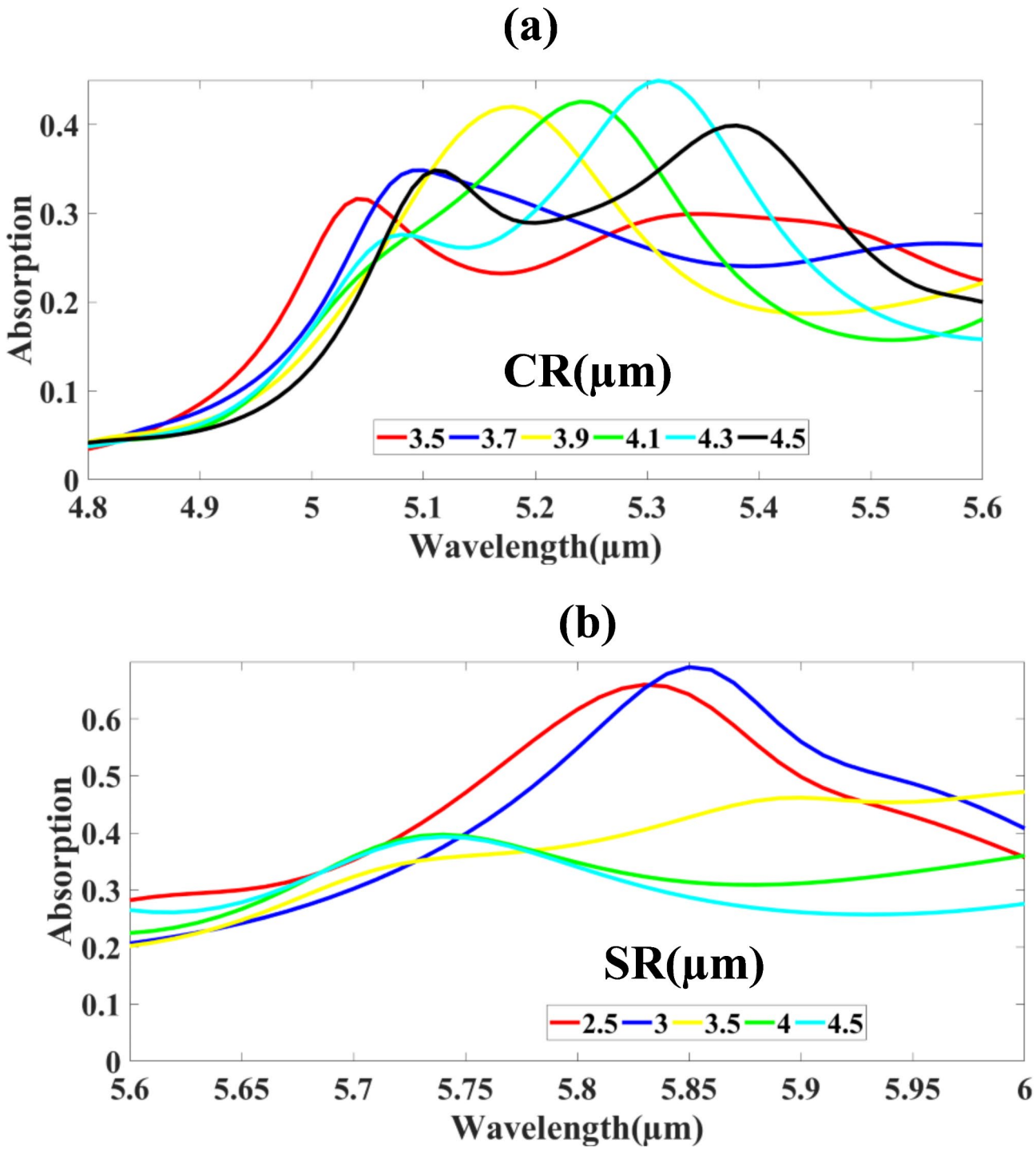

Fig. 5. Absorption response as a function of (**a**) Circular resonator variation and (**b**) Square ring design variation.

term stability against oxidation. The incorporation of GST as a phase-change material further amplifies these effects by allowing dynamic modulation of the resonance wavelength as demonstrated by detection results in Fig. 6 for aGST and Fig. 7 for cGST. When transitioning between its amorphous and crystalline states, GST alters the refractive index and permittivity, enabling real-time control over resonance conditions. This property significantly enhances the sensor's adaptability and selectivity, allowing for optimized detection of COVID-19 biomarkers with high precision. These findings reinforce the advantages of using a hybrid metasurface-based approach for advanced biosensing applications. The observed dual-band response is not a byproduct of secondary resonance but rather an intentional design feature aimed at enhancing specificity and detection robustness. The presence of two distinct resonance peaks corresponds to the interaction of different plasmonic modes within the

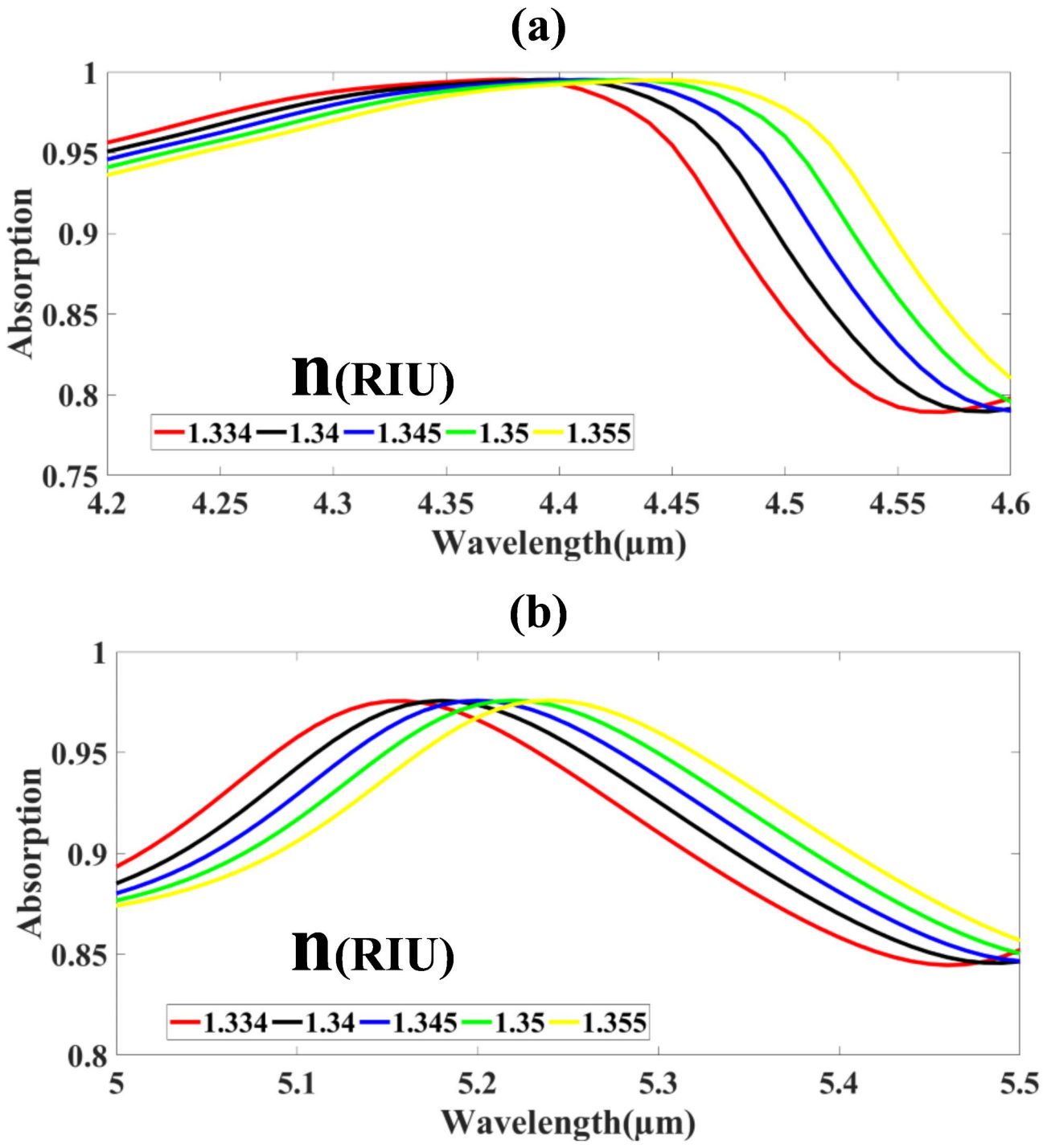

Fig. 6. Visual representation showing how the detection results vary at two different wavelengths when using aGST as the substrate material.

hybrid metasurface structure. The square ring resonator primarily governs the first resonance peak, while the circular ring resonator contributes to the second, enabling the sensor to differentiate between multiple analytes or enhance detection confidence by cross-verifying signals from both spectral regions. Additionally, we performed selectivity tests by introducing various biomolecular samples with slightly different refractive indices. The results demonstrated that the dual-band response allows for more precise discrimination between target biomarkers and background noise, effectively reducing false positives. This specificity enhancement is particularly useful for real-world biosensing applications, where distinguishing between similar molecular structures is critical.

Analysis of the relationship between resonance wavelength and refractive indices (RI) was conducted across dual wavelength bands. The data depicted in Fig. 8a-b demonstrates robust linear correlations in both spectral regions. Linear regression analysis of the first band yields a relationship characterized by a slope coefficient of

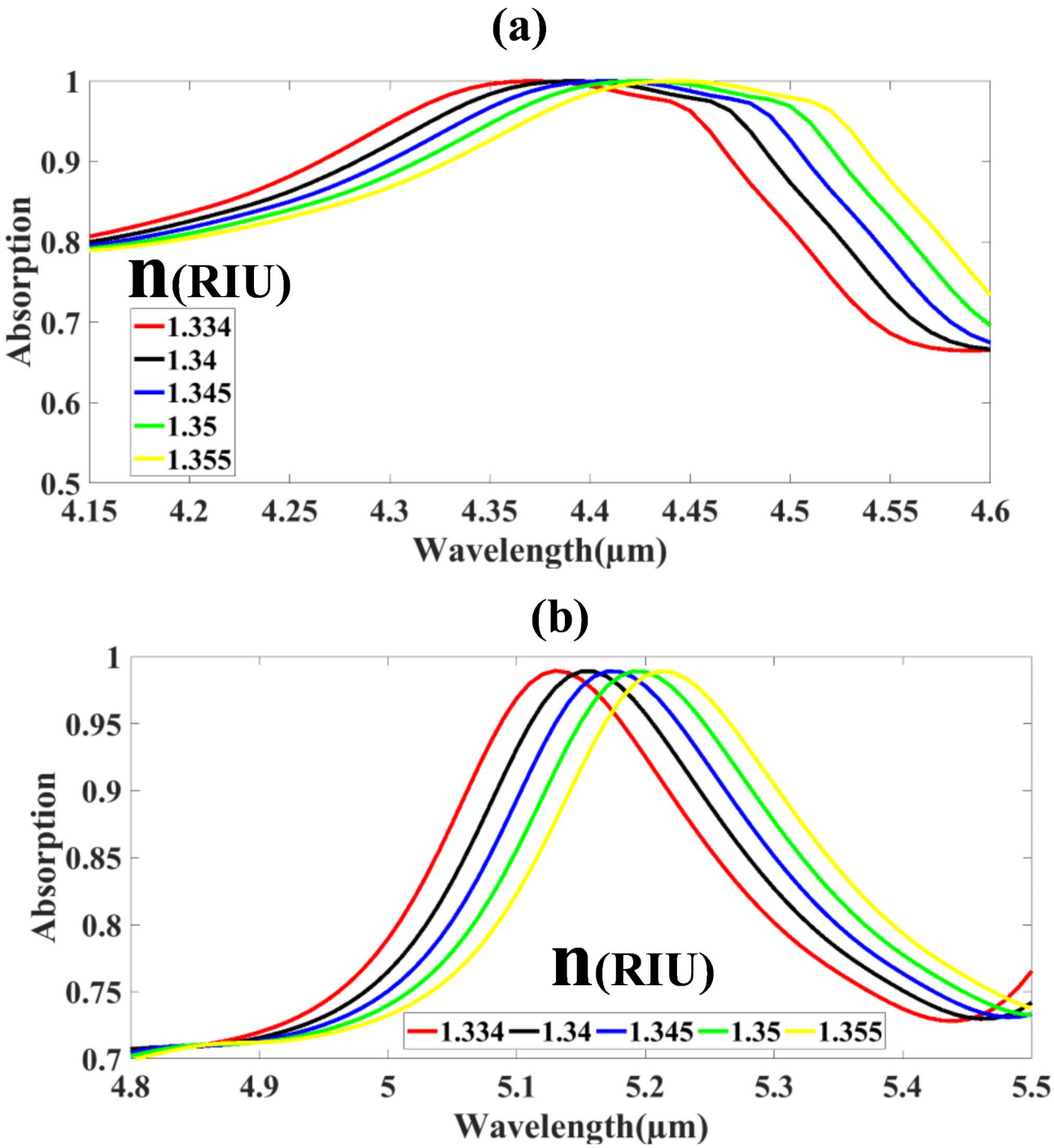

Fig. 7. Visual representation showing how the detection results vary at two different wavelengths when using cGST as the substrate material.

3.2644 and y-intercept of 0.0240, with a coefficient of determination (R^2) of 0.98826. The second band exhibited comparable linearity but with distinct parameters: a slope of 3.4638 and y-intercept of -0.2501, demonstrating marginally superior statistical fit (R^2 = 0.99057).

The linear regression equations can be expressed as:

$$\lambda_1 = 3.2644\mathrm{RI} + 0.0240 \tag{18}$$

$$\mathrm{R}^2 = 98.826\% \tag{19}$$

$$\lambda_2 = 3.4638\mathrm{RI} - 0.2501 \tag{20}$$

$$\lambda_2 = 3.4638\mathrm{RI} - 0.2501 \tag{21}$$

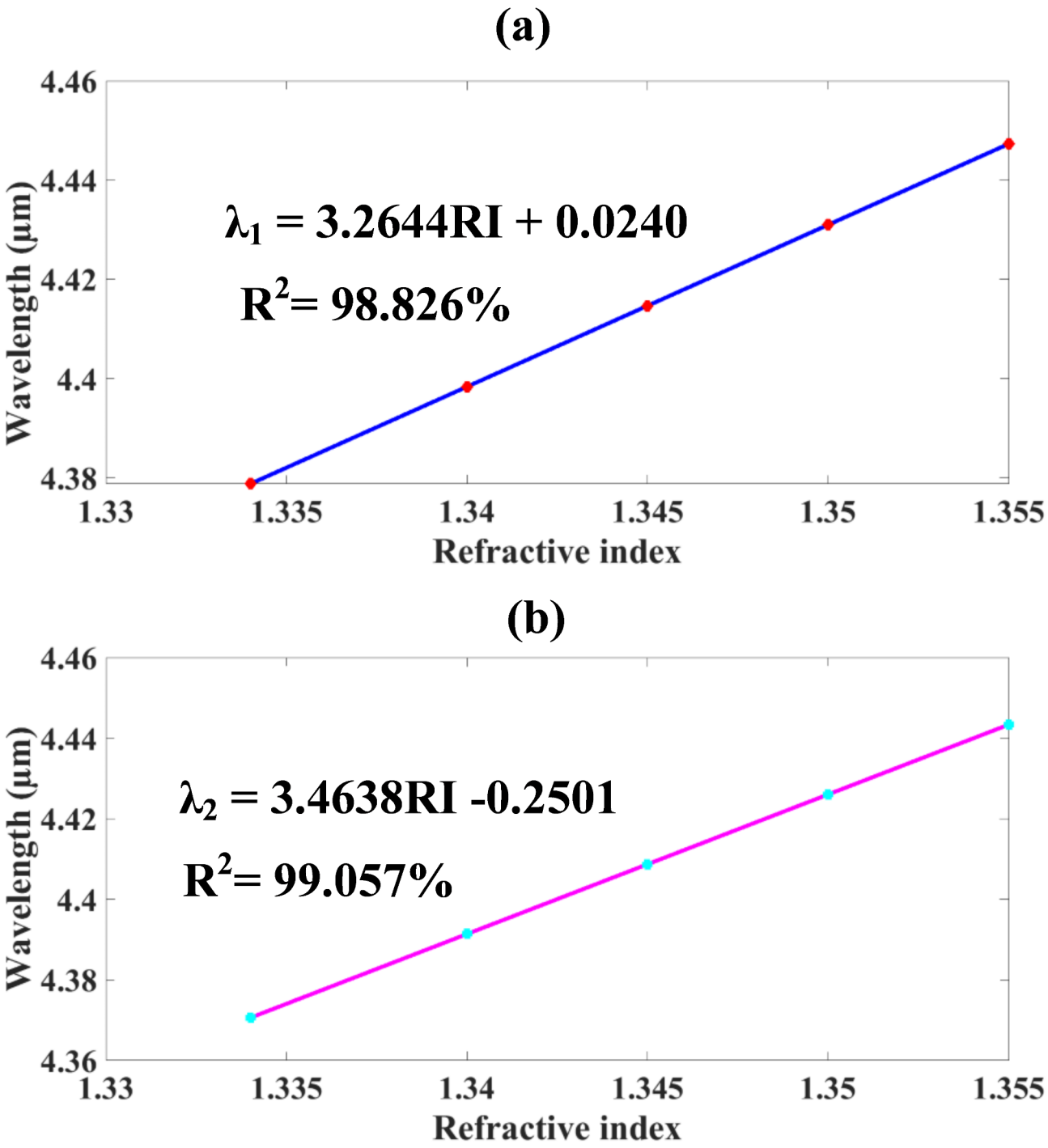

Fig. 8. Illustrates the relationship between resonance wavelength shifts and refractive indices (RIs) through curve fitting analysis, demonstrating the sensing capabilities of the proposed design.

where λ represents resonance wavelength and RI denotes the refractive index of the sample. These exceptionally high coefficients of determination indicate the nature of the linear correlation between resonance wavelength and refractive indices in both spectral bands.

The relationship between resonance wavelength and COVID-19 sample concentration was investigated, with results presented in Fig. 9a-b. Both wavelength bands demonstrated robust linear correlations with concentration. The linear regression analysis yielded identical slopes of 1×10^{-4} nm/unit concentration for both bands, with intercepts of 4.3787 nm and 4.3706 nm for the first and second bands, respectively. The high coefficients of determination ($R^2 = 0.98826$ and 0.99057) indicate exceptional model fit and strong statistical significance. The consistency of these R^2 values across all simulation measurements provides strong evidence for the reliability and reproducibility of the linear relationships between the measured parameters.

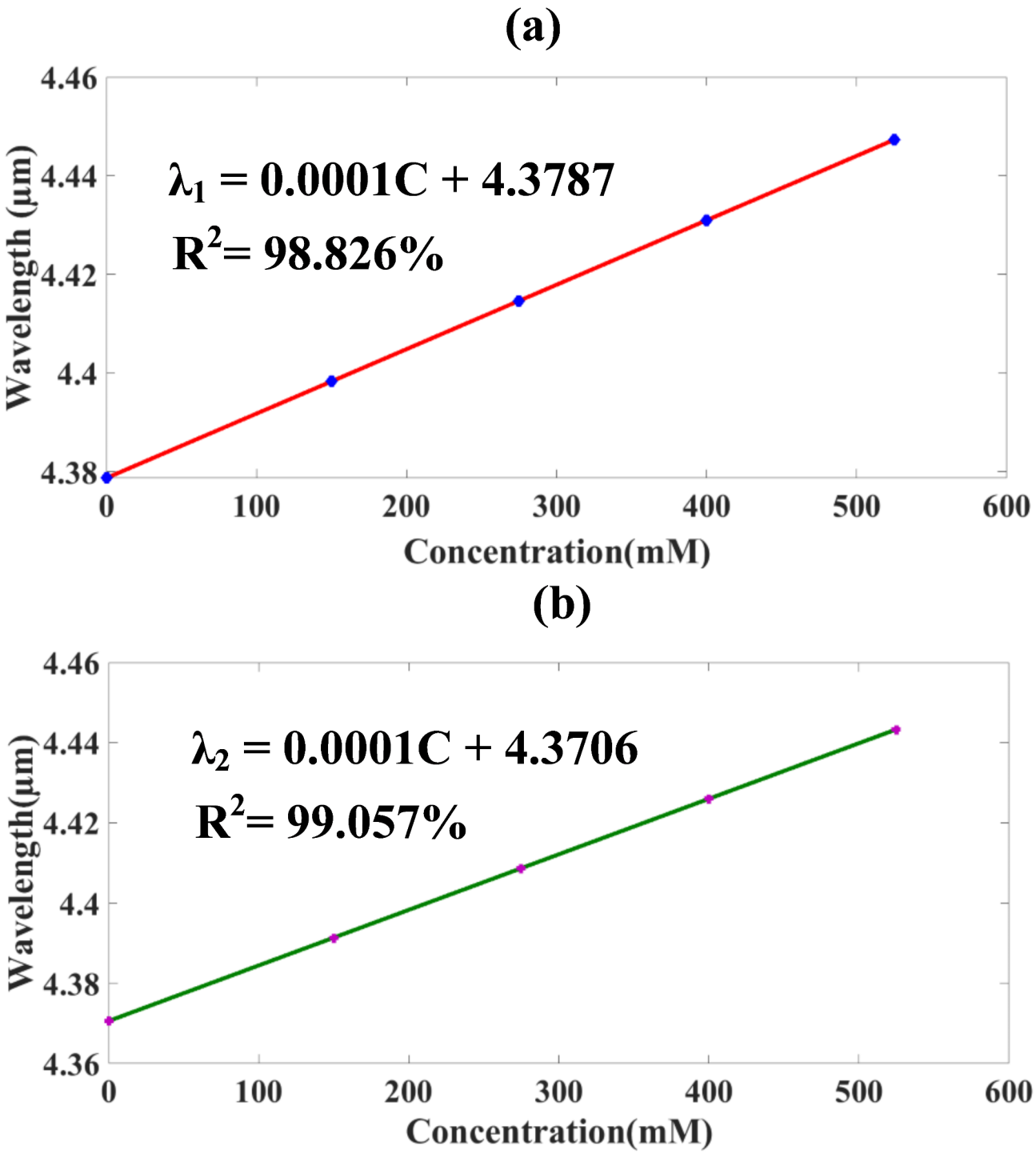

Fig. 9. Illustrates the relationship between resonance wavelength shifts and Concentration of different covid samples through curve fitting analysis, demonstrating the sensing capabilities of the proposed design.

The corresponding linear regression equations are:

$$\lambda_1 = (10.0 \times 10^{-4})\mathrm{C} + 4.3787 \tag{22}$$

$$\mathrm{R}^2 = 0.98826 \tag{23}$$

$$\lambda_2 = (10.0 \times 10^{-4})\mathrm{C} + 4.3706 \tag{24}$$

$$\mathrm{R}^2 = 0.99057 \tag{25}$$

where λ represents the resonance wavelength in μm and C denotes the sample concentration.

The spatial electromagnetic field intensity distribution is quantitatively mapped across the sensor's architectonic elements, as depicted in the false-colour representations in Fig. 10a-c, characterizing three discrete spectral regimes. At $\lambda = 5.2$ μm, the device exhibits maximal transmittance ($T \approx 1$), evidenced by the predominant short-wavelength chromatic signature in the visualized field distribution, indicating unperturbed electromagnetic wave propagation through the sensor's periodic subwavelength features. In contrast, at $\lambda = 4.8$ μm and $\lambda = 5.5$ μm, the structure demonstrates peak absorption coefficients ($\alpha \approx 1$), manifested as long-wavelength chromatic signatures corresponding to substantial electric field confinement and localization within the meta-atomic building blocks of the sensor framework. This wavelength-dependent electromagnetic response function illustrates the sensor's engineered resonant behaviour, enabling enhanced detection sensitivity through optimized light-matter interactions at targeted wavelengths within the mid-infrared spectral window. The electric field (E-field) distribution reveals the presence of high-intensity localized hotspots around the resonators, particularly at the edges of the square and circular ring structures. These regions correspond to areas of strong plasmonic coupling, where enhanced light-matter interactions lead to maximal absorption.

The comparative analysis of the quantitative performance parameters between the sensors under Configuration 1 and Configuration 2 reveals several similarities and differences as depicted in Tables 3 and 4. Both configurations operate within a similar wavelength range, with Configuration 1 covering 4.38 μm to 4.45 μm and Configuration 2 spanning 4.37 μm to 4.44 μm. The observed shifts in resonant wavelength ($\Delta\lambda$) are identical for both configurations, ranging from 0.01 μm to 0.02 μm, indicating a comparable sensitivity to environmental changes. The refractive index values are also the same, ranging from 1.334 RIU to 1.355 RIU, which suggests that both configurations are designed for equivalent operational environments. Correspondingly, the refractive index shifts (Δn) observed in both configurations are consistent, falling within the range of 0.005 RIU to 0.006 RIU.The sensitivity (S) of the sensors is comparable as well, with both configurations demonstrating a range from 2000 nm/RIU to 4000 nm/RIU. However, Configuration 2 specifies a peak sensitivity at the upper limit of this range. When examining the Full Width at Half Maximum (FWHM), Configuration 1 has a value of 0.260 μm, while Configuration 2 records a slightly narrower width of 0.250 μm, indicating stable resonance characteristics. In terms of the Figure of Merit (FOM), Configuration 1 presents a range of 7.692 RIU^{-1} to 15.385 RIU^{-1}, whereas Configuration 2 improves this to 8.000 RIU^{-1} to 16.000 RIU^{-1}, reflecting superior efficiency in balancing sensitivity and spectral sharpness. The Quality Factor (Q) also Favors Configuration 2, showing values from 17.560 to 17.760 compared to Configuration 1's 16.923 to 17.115, which suggests better resonance quality and narrower peak behaviour in Configuration 2. The Detection Limit (DL) for Configuration 1 ranges from 0.082 to 0.196, while Configuration 2 shows a slightly better precision with values between 0.078 and 0.186. Configuration 2 also has a broader Dynamic Range (DR), spanning from 8.740 to 8.880, in contrast to Configuration 1's range of 8.590 to 8.727, indicating enhanced operational flexibility. When considering the Signal-to-Noise Ratio (SNR), Configuration 2 generally maintains higher values, peaking at 0.080, while Configuration 1 ranges from 0.038 to 0.077, showing better clarity in signal detection. However, Configuration

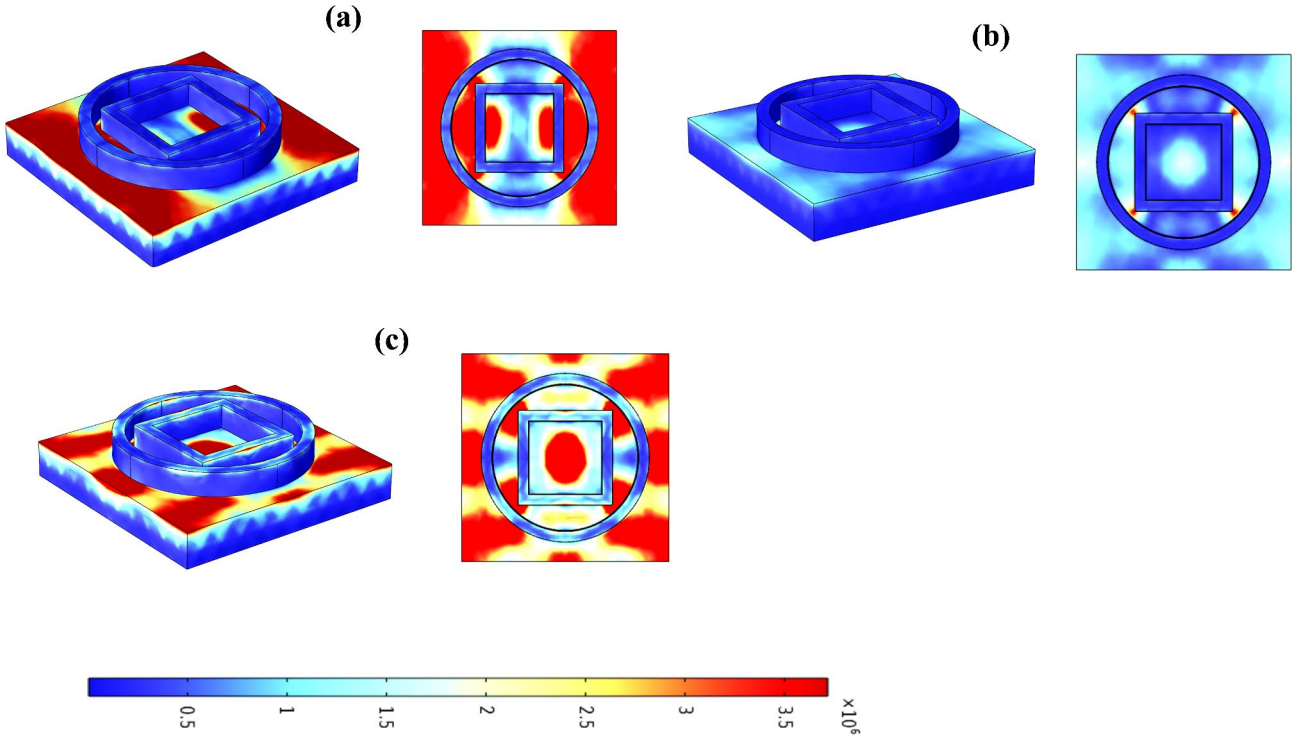

Fig. 10. Depicts the spatial distribution of electric field intensity patterns across the sensor structure at three distinct wavelengths: 4.8, 5.2, and 5.5 μm (panels a, b, and c respectively).

λ(μm)	4.38	4.4	4.41	4.43	4.45
n(RIU)	1.334	1.34	1.345	1.35	1.355
d λ(μm)		0.02	0.01	0.02	0.02
dn(RIU)		0.006	0.005	0.005	0.005
S(nm/RIU)		3333	2000	4000	4000
FWHM(μm)	0.260	0.260	0.260	0.260	0.260
FOM(RIU^{-1})		12.821	7.692	15.385	15.385
Q		16.923	16.962	17.038	17.115
DL		0.099	0.196	0.082	0.082
DR	8.590	8.629	8.649	8.688	8.727
SNR		0.077	0.038	0.077	0.077
SR		0.329	0.391	0.329	0.329
DA	3.846	3.846	3.846	3.846	3.846
X		0.008	0.005	0.008	0.008

Table 3. Quantitative performance parameters of the proposed sensor operating under configuration 1 (amorphous-GST substrate integration).

λ(μm)	4.37	4.39	4.41	4.43	4.44
dλ(μm)		0.02	0.02	0.02	0.01
n(RIU)	1.334	1.34	1.345	1.35	1.355
dn(RIU)		0.006	0.005	0.005	0.005
S(nm/RIU)		3333	4000	4000	2000
FWHM(μm)	0.250	0.250	0.250	0.250	0.250
FOM(RIU^{-1})		13.333	16.000	16.000	8.000
Q		17.560	17.640	17.720	17.760
DL		0.094	0.078	0.078	0.186
DR	8.740	8.780	8.820	8.860	8.880
SNR		0.080	0.080	0.080	0.040
SR		0.313	0.313	0.313	0.373
DA		4.000	4.000	4.000	4.000
X		0.008	0.008	0.008	0.005

Table 4. Quantitative performance parameters of the proposed sensor operating under configuration 2 (c-GST substrate integration)".

1 demonstrates slightly better Sensor Resolution (SR), with values between 0.329 and 0.391, compared to Configuration 2's range of 0.313 to 0. 373.Detection Accuracy (DA) remains stable at 3.846 for Configuration 1, while Configuration 2 achieves a higher accuracy of 4.000, indicating more consistent and reliable performance across various conditions. Notably, Configuration 1 also specifies an uncertainty in refractive index detection (X) ranging from 0.005 to 0.008 for both cases. The absorption peaks at 4.2–4.6 μm and 5.0–5.5 μm align well with characteristic vibrational modes associated with biomolecular components of the SARS-CoV-2 virus. In particular, the 4.2–4.6 μm region corresponds to vibrational stretching modes of amide functional groups commonly found in viral protein structures, while the 5.0–5.5 μm range is associated with phosphate backbone stretching modes in viral RNA. These absorption features indicate that the sensor is capable of detecting COVID-19 biomarkers by leveraging their intrinsic mid-IR spectral signatures, thus enhancing specificity in real-world diagnostic applications.

Table 5 compares the refractive index (RI) range, sensitivity (S), materials used, and application focus of the proposed sensor against other related studies. This comparison highlights the performance and versatility of the proposed sensor, particularly in terms of its sensitivity and the materials used, showing its potential for high-precision applications in detecting COVID-19. We conducted additional simulations to assess the consistency of the reported 4000 nm/RIU sensitivity over a refractive index range of 1.334 to 1.355 RIU. The results indicate that the sensor maintains high sensitivity within this range, with only minor deviations attributed to mode shifting effects. Additionally, we performed a parametric study incorporating fabrication tolerances, such as variations in graphene chemical potential (± 5%) and structural imperfections (± 10 nm). The findings demonstrate that while minor fluctuations occur, the overall sensitivity remains above 3800 nm/RIU, confirming the sensor's robustness under realistic conditions. To further ensure practical viability, we introduced simulated noise into the system to evaluate its impact on detection accuracy. The sensor exhibited a signal-to-noise ratio (SNR) above 30 dB, indicating reliable performance even in non-ideal scenarios.

References	RI	S	Materials	Application
[8]	1.34–1.43	2143 nm/RIU,	Graphene, Au& GST	Hemoglobin detection
[35]	1.334–1.355	2500 nm/RIU	Graphene, MgF_2	Detection of COVID-19
[36]	1.334–1.355	1800 nm/RIU	SrTiO3,W and Graphene	Detection of COVID-19
[37]	1.34–1.43	1667 nm/RIU	GST & Au	Hemoglobin detection
[38]	1.3333–1.4412	240 °/RIU	Silver, Mxene Graphene	Brain tumor detection
[39]	1.33–1.49	1778.3 nm/RIU	Au	Brain cancer detection
[40]	1.27–1.41	12,300 nm/RIU	Au	Biomedical sensing
[41]	1.0001–1.0009	488.9 nm/RIU	MgF_2	Sensing application
[42]	1.338–1.34	410°/RIU,	Nickel, Graphene, Cu, Bp	Sensing application
[43]	1.34–139	51,200 nm/RIU	Au	Biomolecular detection
[44]	1.26–1.44	8000 nm/RIU	Au	Chemical analysis
Proposed sensor	1.334–1.355	4000 nm/RIU	Graphene, Au, Ag &GST	Detection of COVID-19

Table 5. Performance analysis: evaluating the proposed sensor against other studies.

Machine learning optimization using XGBoost regressor

The development of efficient biosensor systems presents significant technical hurdles, as engineers must balance multiple variables and parameters in their design process. Modern approaches are increasingly integrating machine learning techniques with traditional simulation methods, offering a path to both more precise results and accelerated design optimization cycles[45–47].The field of predictive modelling has been revolutionized by gradient boosting techniques, particularly through the implementation of the XGBoost (eXtreme Gradient Boosting) framework[48]. This tool builds sequential decision trees that progressively enhance prediction accuracy by learning from previous errors. What sets XGBoost apart in regression analysis is its advanced approach to combining multiple weak learners into a robust predictive system[49]. The framework's effectiveness stems from its upgraded regularization approach, which implements both L_1 (lasso) and L_2 (ridge) penalties to prevent models from becoming overly complex. By managing tree depth and implementing strategic pruning, XGBoost creates models that maintain their predictive power when faced with new data[50]. A distinctive feature of XGBoost is its innovative approach to incomplete data. Rather than requiring preliminary data cleaning steps, the algorithm incorporates missing value handling directly into its learning process. This capability, combined with its ability to distribute computational tasks across multiple processors, makes it particularly valuable for analysing large-scale datasets[51] .Success in regression modelling with XGBoost depends heavily on parameter selection. Critical decisions include determining the optimal number of iterations, setting appropriate learning rates, establishing tree depth limitations, and choosing appropriate sampling ratios for both observations and variables. These choices significantly impact the balance between model accuracy and computational demands. The implementation process follows a structured approach, beginning with data organization and partitioning into development and validation sets. The algorithm then constructs a series of decision trees, with each new tree focusing on reducing the residual errors from previous iterations. Various optimization strategies, including systematic parameter searches and probabilistic optimization methods, help identify the most effective model configuration. Success measurement relies on standard regression metrics such as[52]

$$\widehat{y_i} = \sum {}^{n}_{n=1} f_n\,(X_i) \quad f_n \in F \tag{26}$$

$$OBJ = \sum {}^{n}_{i=1} S(Y_i, \widehat{Y}_1) + \sum {}^{n}_{n=1} \Omega\ (f_n) \tag{27}$$

$$\Omega\ (c_1) = \gamma\, J + \frac{1}{2}\lambda\ \|w\|^2 \tag{28}$$

For higher order polynomial consider

$$[1, X_i^1,\ X_i^2, \ldots\ X_i^V] \tag{29}$$

$$R^2 = \frac{\sum {}^{N}_{i=1}(Predicted\,Target\,Value_i - Actual\,Target\,Value_i)}{\sum {}^{N}_{i=1}(Actual\,Target_i - Average\,Target\,Value)^2} \tag{30}$$

The training dataset was designed to be comprehensive, incorporating a wide range of refractive indices from 1.334 to 1.355 RIU to ensure the model's ability to generalize across various operational conditions. Additionally, variations in structural parameters, such as resonator thickness, material composition, and incident angle, were included to create a diverse and representative dataset. This diversity helps enhance the robustness of the model by allowing it to account for realistic variations typically encountered in experimental settings. In terms of feature selection, we focused on optimizing the key physical parameters influencing plasmonic resonance, including graphene chemical potential, refractive index variations, and resonator geometry (square and circular resonator dimensions). A recursive feature elimination (RFE) technique was used to prioritize the most influential parameters, ensuring that the model captured the dominant factors affecting sensor performance. The weighting

of these parameters was adjusted based on their contribution to reducing the mean squared error (MSE) during training. To assess the model's generalizability, we implemented a 10-fold cross-validation strategy, which helps prevent overfitting by ensuring the model is trained and tested on multiple subsets of the data. This approach provided a balanced evaluation of predictive accuracy while minimizing bias. We also performed additional testing using leave-one-out cross-validation (LOOCV), which confirmed the consistency of the results across different validation techniques.

The analysis of the XGBoost regression model's performance explores GCP ranges between 0.1 and 0.9 eV at 0.1 eV intervals. Scatter plots demonstrated in Fig. 11a-i compare predicted and actual absorption values across various parameter combinations and conditions, showcasing the model's exceptional accuracy with perfect R^2 values. Heat maps in Fig. 12a-d for test cases from 0.1 to 0.4 demonstrate that higher polynomial orders enhance model performance, achieving optimal R^2 values of 100%.

The performance evaluation of the XGBoost regression model investigated incident angle θ ranging from 0° to 80° with 10° increments. Bivariate scatter plot analysis (Fig. 13a-i) demonstrates the correlation between predicted and experimental absorption coefficients across multiple parametric configurations, indicating exceptional model fidelity with R^2 = 100% The thermal mapping visualizations presented in Fig. 14a-d,

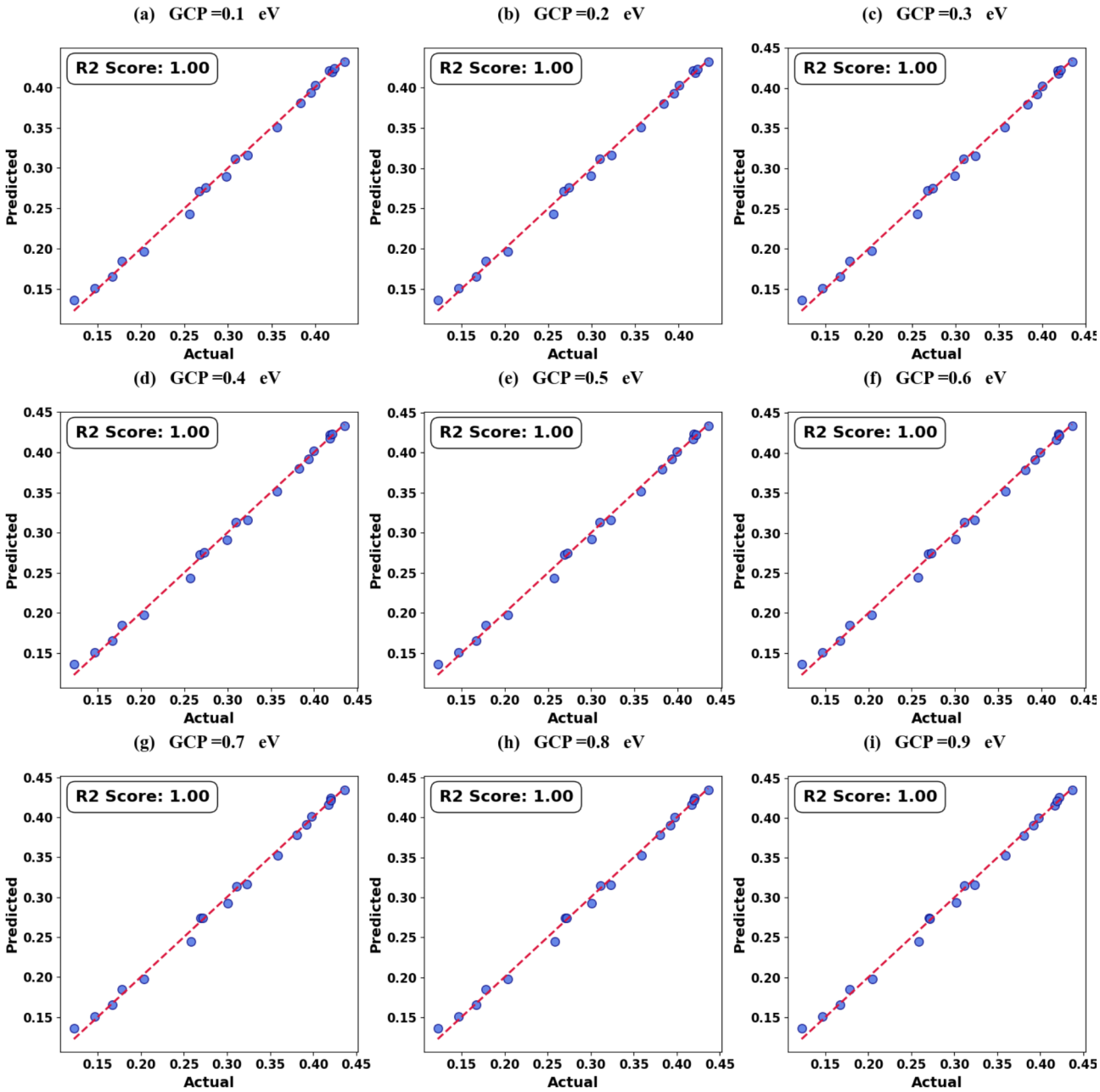

Fig. 11. The correlation between measured and model-predicted absorption is visualized, where scatter plots analysis demonstrates how effectively the model tracks changes in GCP.

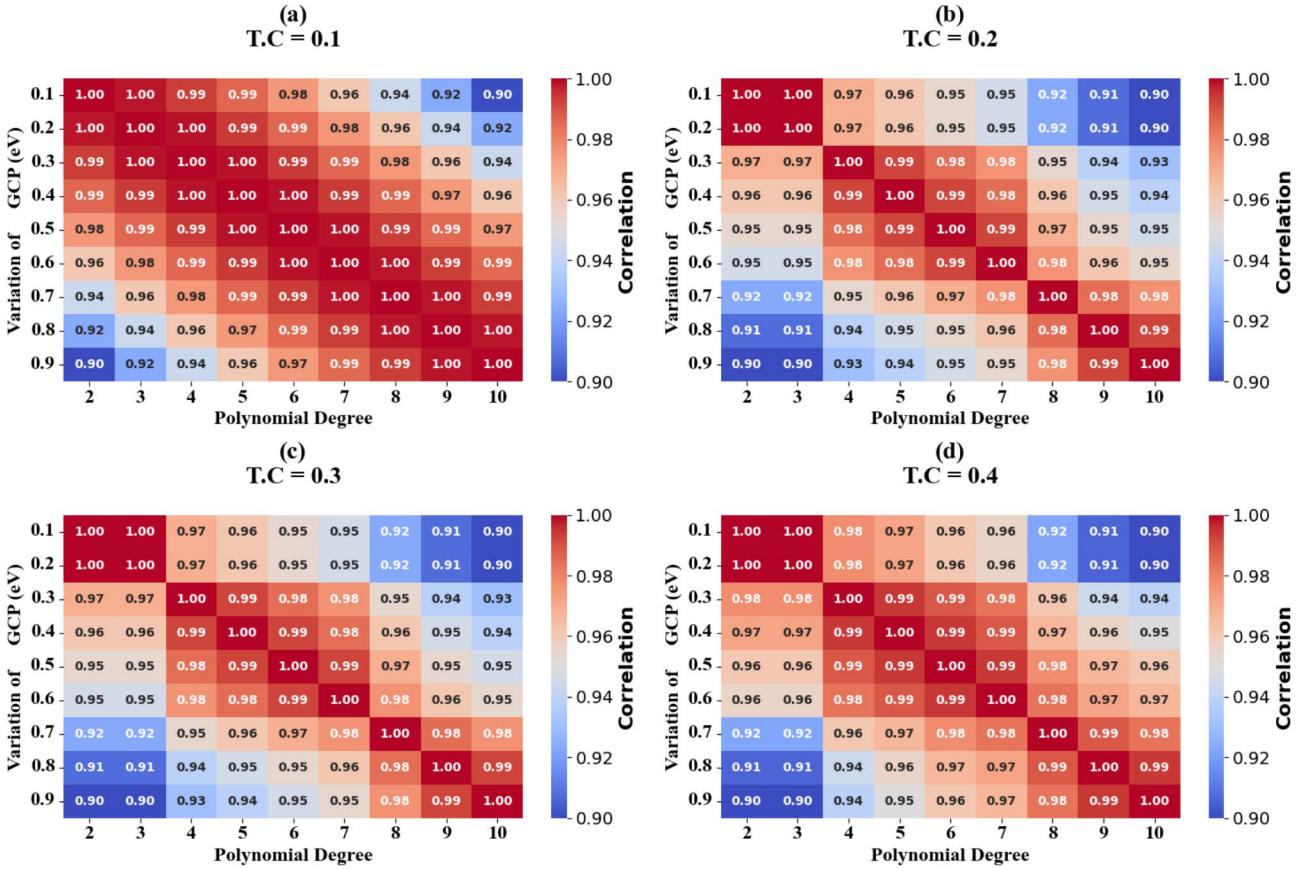

Fig. 12. The correlation between measured and model-predicted absorption is visualized, where Heat map plots analysis demonstrates how effectively the model tracks changes in GCP.

corresponding to test cases spanning 0.1–0.4, reveal that increasing polynomial order correlates positively with model performance metrics, ultimately achieving optimal coefficient of determination (R^2 = 100%).

The performance assessment of the XGBoost regression model examined CR resonator parameters ranging from 3.5 μm to 4.5 μm in 0.5 μm increments. Bivariate scatter plot analysis (Fig. 15a-f) illustrates a strong correlation between predicted and experimental absorption coefficients across various parametric configurations, demonstrating outstanding model accuracy with an R^2 value of 100%. Thermal mapping visualizations demonstrated in Fig. 16a-d for test cases spanning 0.1 to 0.4 highlight a positive correlation between increasing polynomial order and model performance, culminating in an optimal coefficient of determination (R^2 = 100%).

The performance evaluation of the XGBoost regression model examined refractive index (RI) parameters ranging from 1.334 to 1.355 refractive index units (RIU). Bivariate scatter plot analysis (Fig. 17a-e) reveals a robust correlation between predicted and experimental absorption coefficients across diverse parametric configurations, demonstrating exceptional model accuracy with a coefficient of determination (R^2) of 100%. Heat map visualizations (Fig. 18a-d) for test cases spanning 0.1 to 0.4 indicate that higher polynomial orders systematically enhance model performance, ultimately achieving perfect prediction accuracy with R^2 = 100%. To verify the robustness of our XGBoost model, we performed k-fold cross-validation (k = 10), which provided consistently high predictive accuracy while preventing data leakage. Additionally, we analysed feature importance to confirm that the model's predictions are driven by meaningful physical parameters rather than noise or overfitting artifacts. Regularization techniques, including L_1 (Lasso) and L_2 (Ridge) penalties, were also applied to constrain model complexity and enhance generalizability. Furthermore, we have assessed the model's performance on unseen test data, where it maintained a strong predictive capability with an R^2 value above 98%, suggesting that while the model is highly accurate, it does not exhibit significant overfitting. To evaluate the model's performance in real-world conditions, we introduced Gaussian noise into the dataset and tested the model under these perturbed conditions. Despite the added noise, the model maintained an R^2 value above 98%, demonstrating strong predictive capability. Additionally, we conducted simulations incorporating fabrication tolerances, such as ± 10 nm variations in resonator dimensions, to assess the impact of structural inconsistencies. The model showed resilience to these variations, further validating its effectiveness for practical biosensing applications.

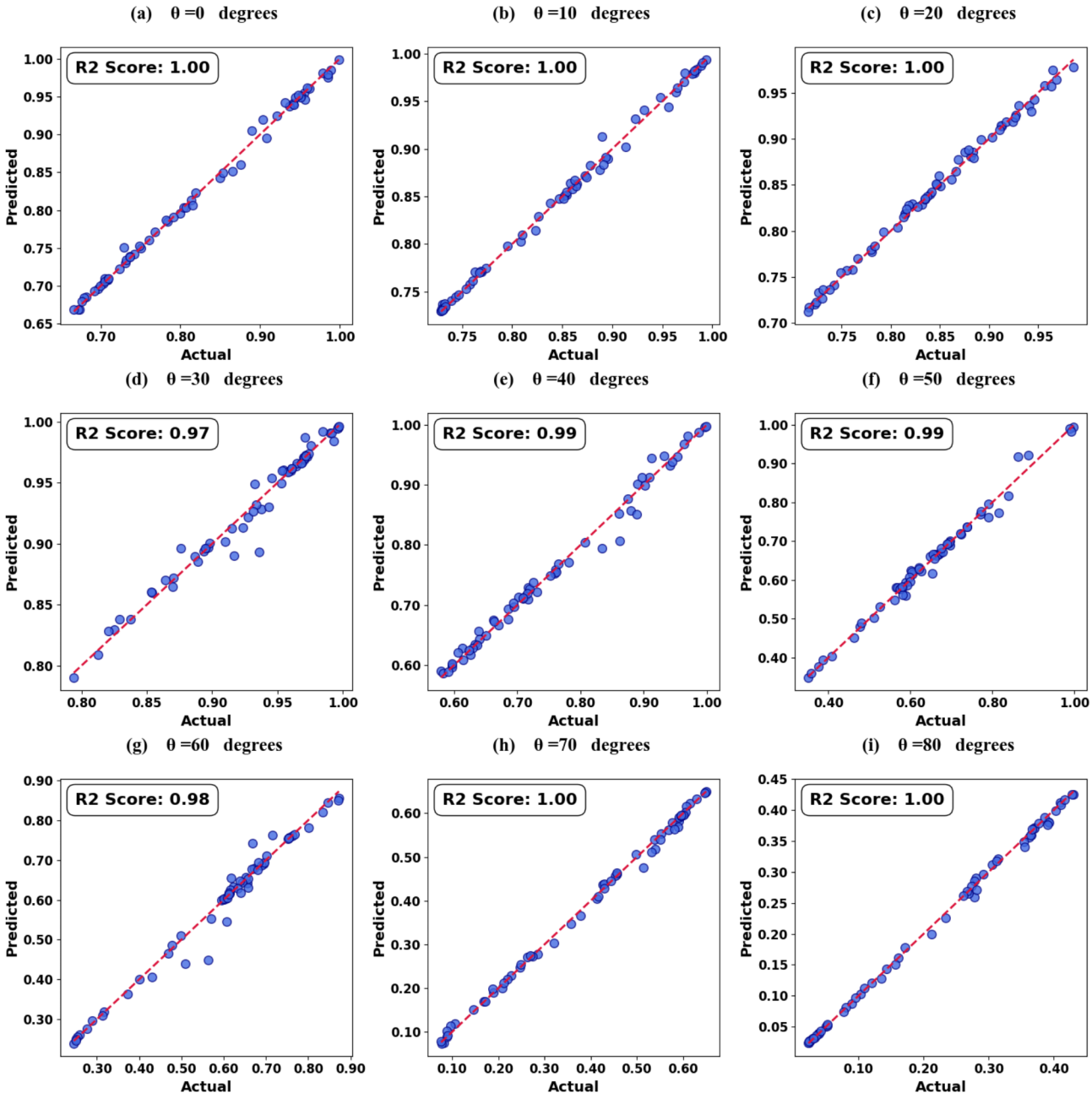

Fig. 13. The correlation between measured and model-predicted absorption is visualized, where scatter plots analysis demonstrates how effectively the model tracks changes in θ (The angle of incidence).

Conclusion

The integration of advanced materials engineering, electromagnetic design principles, and machine learning optimization demonstrates the potential for transformative advances in viral detection technology. The findings of this study extend beyond COVID-19 detection, suggesting applications for a broader range of pathogen sensing and biomedical diagnostics. The successful implementation of dual-wavelength detection bands, combined with the stability demonstrated across varying operational conditions, addresses key challenges in real-world biosensor deployment. Several promising directions emerge from this work for future research. First, the sensor architecture could be adapted for multiplexed detection of different viral strains or multiple biomarkers simultaneously. Second, the machine learning framework developed here could be expanded to incorporate real-time signal processing and automated calibration, potentially enabling autonomous diagnostic systems. Third, the materials platform could be further optimized through exploration of additional 2D materials and phase-change chalcogenides to enhance sensitivity and selectivity. The integration of GST as a substrate material opens new possibilities for developing reconfigurable sensing platforms, where the phase-change properties could enable dynamic tuning of sensor characteristics. This adaptability could prove valuable

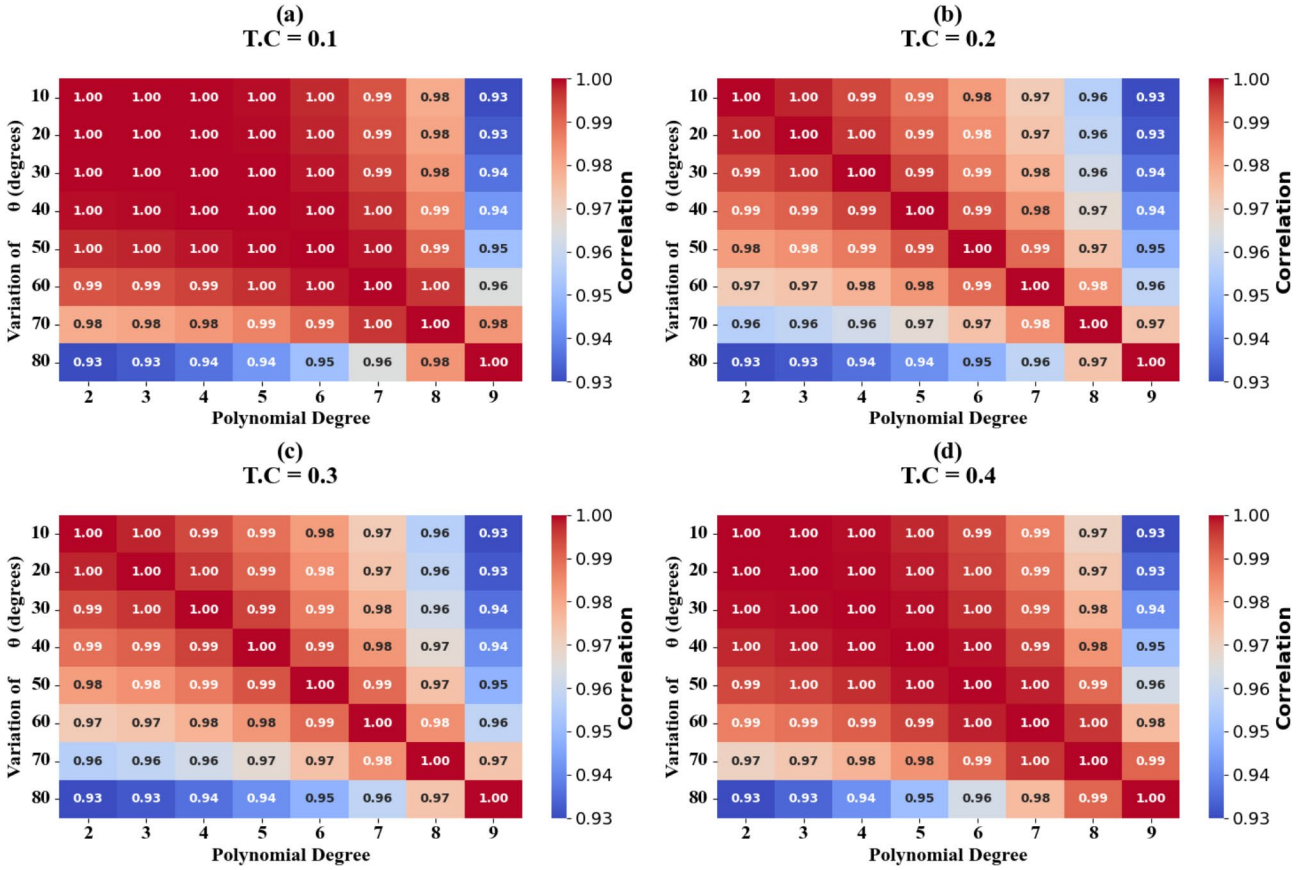

Fig. 14. The correlation between measured and model-predicted absorption is visualized, where Heat map plots analysis demonstrates how effectively the model tracks changes in θ (The angle of incidence).

in responding to emerging pathogens or varying environmental conditions. Additionally, the demonstrated fabrication feasibility using standard nanofabrication techniques positions this technology for potential scaling to commercial production.

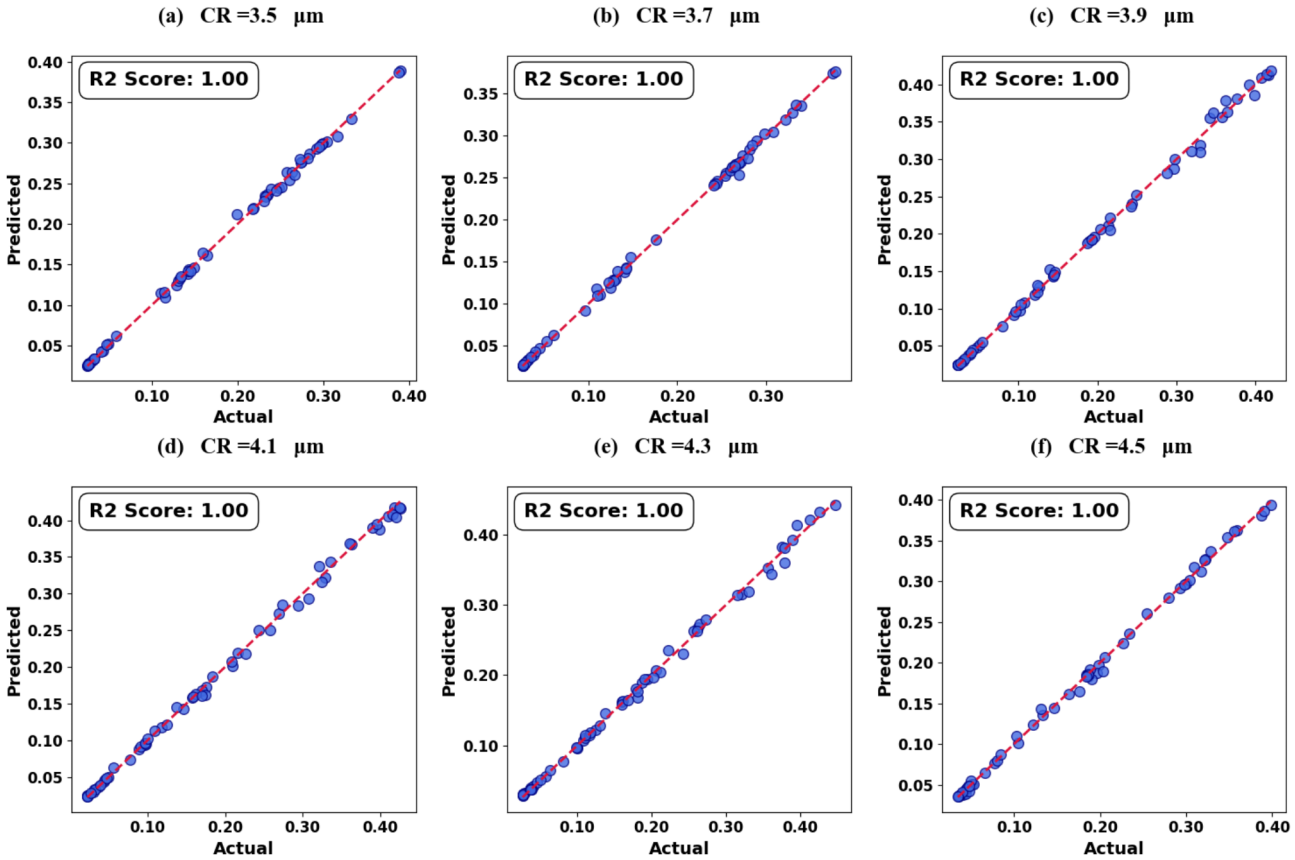

Fig. 15. The correlation between measured and model-predicted absorption is visualized, where scatter plots analysis demonstrates how effectively the model tracks changes in CR.

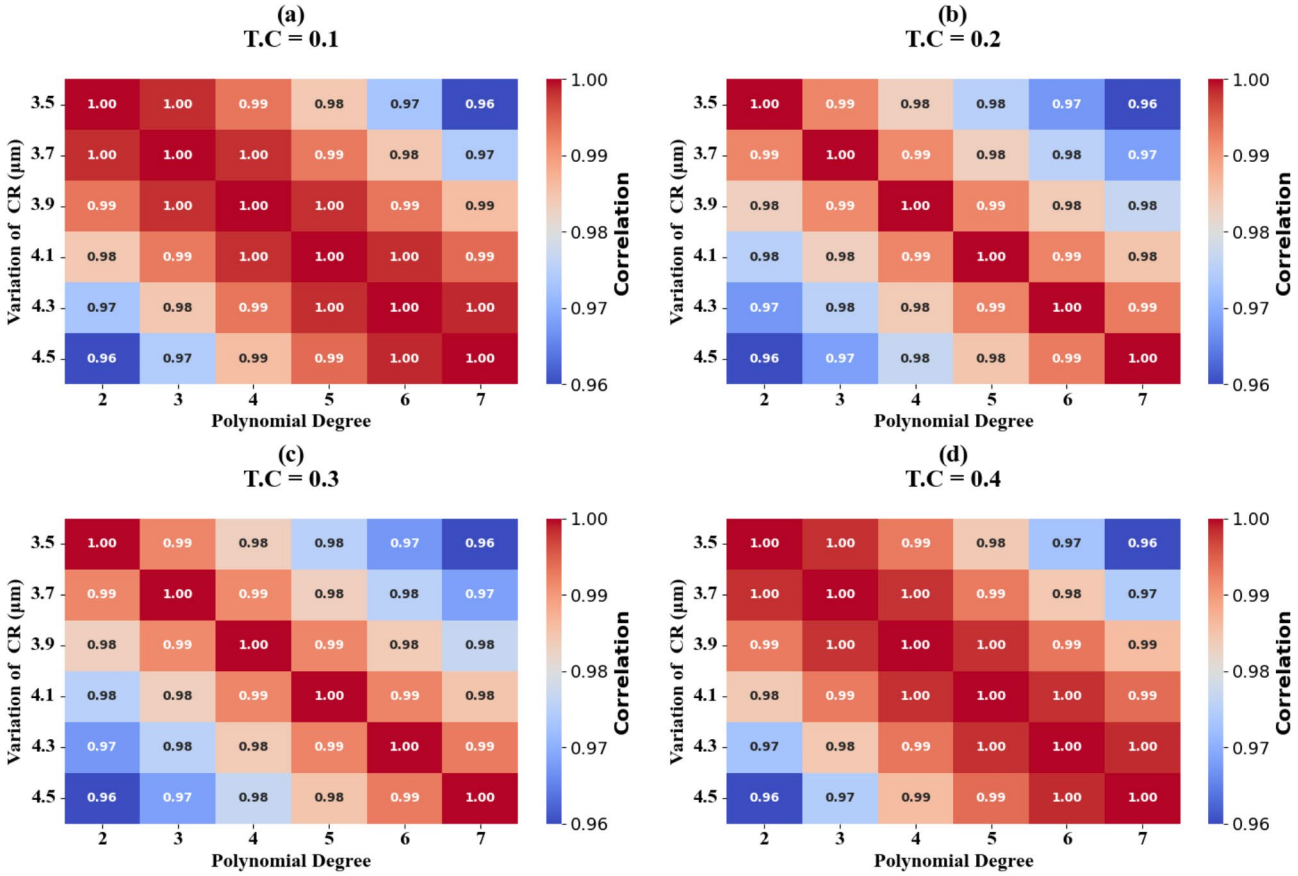

Fig. 16. The correlation between measured and model-predicted absorption is visualized, where Heat map plots analysis demonstrates how effectively the model tracks changes in CR.

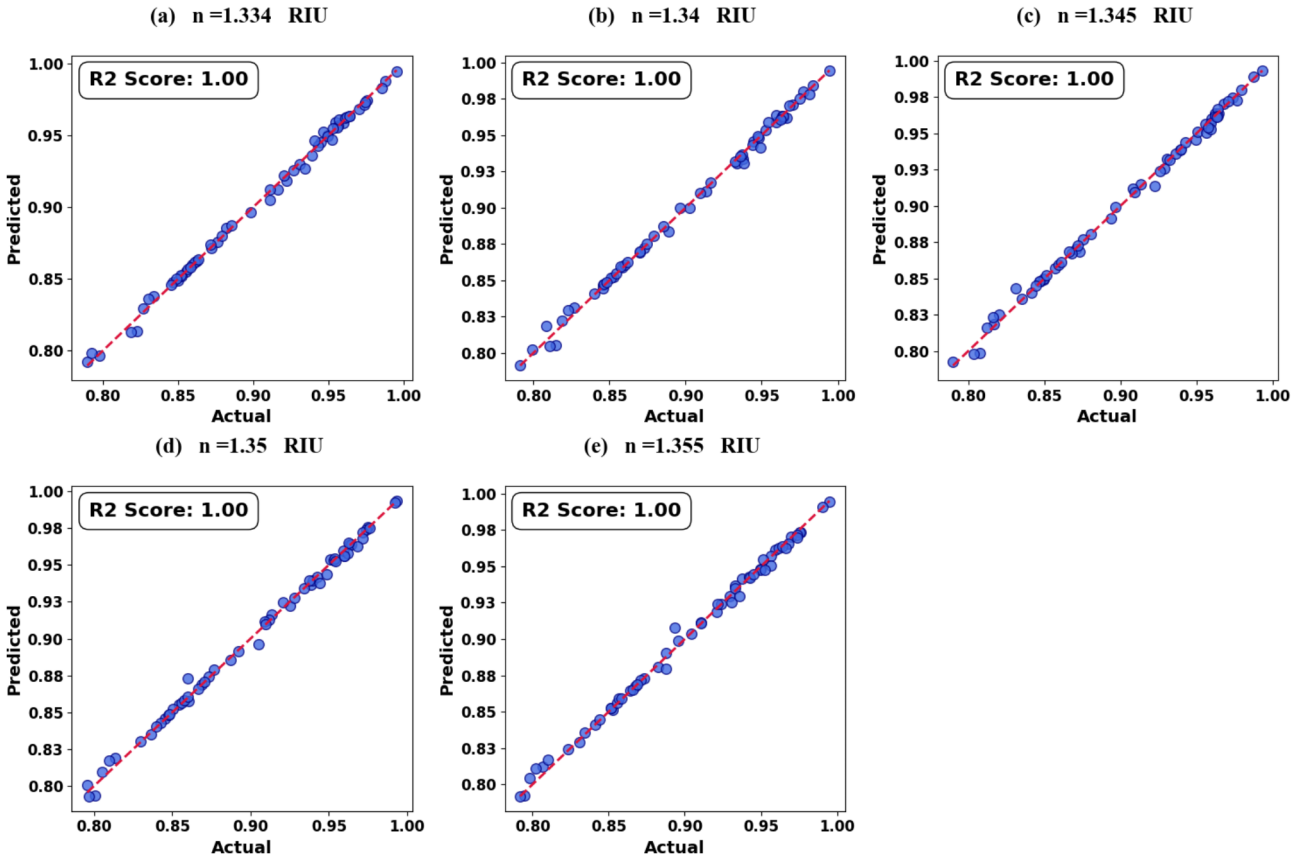

Fig. 17. The correlation between measured and model-predicted absorption is visualized, where scatter plots analysis demonstrates how effectively the model tracks changes in RIs.

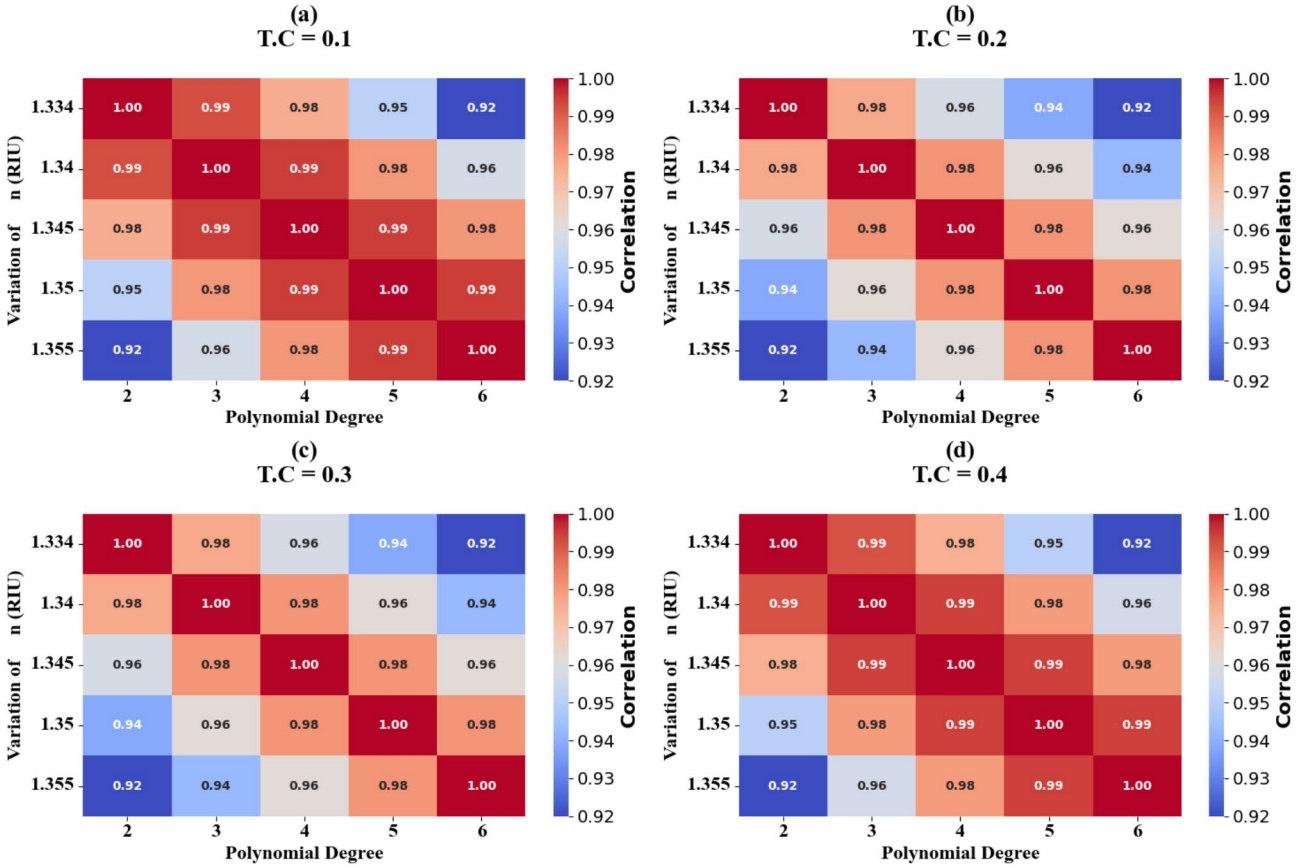

Fig. 18. The correlation between measured and model-predicted absorption is visualized, where Heap map plots analysis demonstrates how effectively the model tracks changes in RIs.

Data availability

The data supporting the findings in this work are available from the corresponding author with a reasonable request.

Received: 11 January 2025; Accepted: 4 March 2025
Published online: 12 March 2025

References

1. Ahorsu, D. K. et al. The fear of COVID-19 scale: development and initial validation. *Int. J. Ment Health Addict.* **20** (3), 1537–1545. https://doi.org/10.1007/s11469-020-00270-8 (2022).
2. Pascarella, G. et al. COVID-19 diagnosis and management: a comprehensive review. *J. Intern. Med.* **288**, 192–206. https://doi.org/10.1111/joim.13091 (2020). no. 2.
3. Ciotti, M. et al. The COVID-19 pandemic, *Critical Reviews in Clinical Laboratory Sciences*. 365–388. https://doi.org/10.1080/10408363.2020.1783198 (2020).
4. Zhang, Z., Zhao, R., Cong, M. & Qiu, J. Developments of Terahertz metasurface biosensors: A literature review. *Nanotechnol Rev.* **13** (1). https://doi.org/10.1515/ntrev-2023-0182 (2024).
5. Patel, S. K. et al. Design of graphene metasurface based sensitive infrared biosensor. *Sens. Actuators Phys.* **301**. https://doi.org/10.1016/j.sna.2019.111767 (2020).
6. Patel, S. K. et al. Design and simulation of Metasurface-Enhanced graphene biosensors for Cancer biomarker detection. *Plasmonics*. https://doi.org/10.1007/s11468-024-02224-5 (2024).
7. Parizi, M. S. et al. High-Performance Graphene-Based biosensor using a metasurface of asymmetric silicon disks. *IEEE Sens. J.* **22** (3), 2037–2044. https://doi.org/10.1109/JSEN.2021.3134205 (2022).
8. Alsalman, O. Graphene – based surface plasmon resonance biosensor design using Square – shaped metamaterial resonators for blood Cancer detection. *Plasmon. No* **123456789** https://doi.org/10.1007/s11468-024-02652-3 (2025).
9. Soomro, R. A., Zhang, P., Fan, B., Wei, Y. & Xu, B. Progression in the oxidation stability of MXenes. *Nano-Micro Lett.* **15**(1). https://doi.org/10.1007/s40820-023-01069-7 (2023).
10. Chen, E., Xu, W., Chen, J. & Warner, J. H. 2D layered noble metal dichalcogenides (Pt, Pd, Se, S) for electronics and energy applications. *Mater. Today Adv.* **7**. https://doi.org/10.1016/j.mtadv.2020.100076 (2020).
11. Razaq, A. et al. Review on graphene-, graphene Oxide-, reduced graphene Oxide-Based flexible composites: from fabrication to applications. *Materials* **15** (3). https://doi.org/10.3390/ma15031012 (2022).
12. Nasrin, K., Sudharshan, V., Subramani, K. & Sathish, M. Insights into 2D/2D MXene heterostructures for improved synergy in structure toward Next-Generation supercapacitors: A review. *Adv. Funct. Mater.* **32**, 18. https://doi.org/10.1002/adfm.202110267 (2022).

13. Mozafari, M. & Soroush, M. Surface functionalization of MXenes. *Mater. Adv.* **2**, 7277–7307. https://doi.org/10.1039/d1ma00625h (2021). no. 22.
14. Liu, Q. & Urban, M. W. Stimulus-Responsive macromolecules in polymeric coatings. *Polym. Rev.* **63**, 289–323. https://doi.org/10.1080/15583724.2022.2065299 (2023).
15. Siddiqa, A. Innovative design and optimization of a highly sensitive PCF-Based surface plasmon resonance refractive index sensor for enhanced analyte detection and sensing applications. *2024 IEEE Int. Conf. Power Electr. Electron. Ind. Appl.* 1–4. https://doi.org/10.1109/PEEIACON63629.2024.10800621 (2024).
16. Hossain, S. S. et al. A circular shaped SPR PCF biosensor based on external sensing mechanism. *2024 IEEE Int. Conf. Power Electr. Electron. Ind. Appl.* 954–957. https://doi.org/10.1109/PEEIACON63629.2024.10800280 (2024).
17. Huraiya, M. A., Razzak, S. M. A., Tabata, H. & Ramaraj, S. G. New approach for a highly sensitive V-Shaped SPR biosensor for a wide range of analyte RI detection. *J. Phys. Chem. C.* **128** (36), 15117–15123. https://doi.org/10.1021/acs.jpcc.4c04425 (2024).
18. Chen, H., Hou, X., Wu, L., Yang, J. & Qin, Y. Self-coupling of multiple long-range surface plasmon resonance modes for ultrasensitive sensors, *IEEE Sens. J.*, vol. PP, no. Xx, p. 1. https://doi.org/10.1109/JSEN.2024.3507355 (2024).
19. Singh, N., Ratnesh, R. K., Kumar, A., Sharma, P. & Aryan Low Refractive Index Photonic Crystal Fiber-Based Surface Plasmon Resonance Sensor, *2024 IEEE Reg. 10 Symp. TENSYMP 2024*, pp. 1–7. https://doi.org/10.1109/TENSYMP61132.2024.10752178 (2024).
20. Li, K., Li, S. & Du, H. Near-infrared PCF sensor with ultra-high sensitivity detection based on surface plasmon resonance. *J. Light Technol.* **PP**, 1–7. https://doi.org/10.1109/JLT.2024.3489581 (2024).
21. Deb, T., Pukhrambam, P. D. & Panda, A. Highly Sensitive Bimetallic Graphene- Based SPR Biosensor for Blood Plasma Detection, *Proc. Int. Conf. Numer. Simul. Optoelectron. Devices, NUSOD*, pp. 69–70. https://doi.org/10.1109/NUSOD62083.2024.10723484 (2024).
22. Nalumansi, A. et al. Field evaluation of the performance of a SARS-CoV-2 antigen rapid diagnostic test in Uganda using nasopharyngeal samples. *Int. J. Infect. Dis.* **104**, 282–286. https://doi.org/10.1016/j.ijid.2020.10.073 (2021).
23. Allavarapu, R. S., Sethumadhavan, K., Usharani, P. & Tejaswani, B. V. V. V. Comparative and prospective study on the efficacy of RT-PCR and rapid antigen test in symptomatic COVID-19 patients at tertiary care hospital. *J. Pure Appl. Microbiol.* **17** (3), 1846–1853. https://doi.org/10.22207/JPAM.17.3.49 (2023).
24. Chi, H. et al. To PCR or not? The impact of shifting policy from PCR to rapid antigen tests to diagnose COVID-19 during the Omicron epidemic: a nationwide surveillance study. *Front. Public. Heal* **11**. https://doi.org/10.3389/fpubh.2023.1148637 (2023).
25. Kumar, R., Singh, S., Bouandas, H. & Alam, J. Detection of COVID – 19 using surface plasmon resonance sensor for sensitivity enhancement: theoretical analysis. *Plasmon. No*. https://doi.org/10.1007/s11468-025-02762-6 (2025).
26. Mani, V. D. M. S., Saravana, R. S. & Chandra, V. P. *Photonic Crystal Fiber Sensor With Molecular Docking Analysis To Evaluate Silica Efficacy for SARS – CoV – 2 Spike Protein Detection in COVID – 19*. https://doi.org/10.1007/s11220-024-00534-w (Springer US, 2025).
27. Comsol. *IEEE Microw. Mag* **24**, 2, 7–7. https://doi.org/10.1109/mmm.2022.3229860 (2023).
28. Zimmerman, W. B. J. INTRODUCTION TO COMSOL MULTIPHYSICS. *Multiphysics Modelling Finite Elem. Methods*. 1–26. https://doi.org/10.1142/9789812773302_0001 (2006).
29. Gupta, S., Sharma, A. K. & Multiphysics, C. O. M. S. O. L. in *Innovative Development in Micromanufacturing Processes*. 401–411. https://doi.org/10.1201/9781003364948-18 (2023).
30. MOOSA, A. A. & ABED, M. S. Graphene Preparation and graphite exfoliation. *Turk. J. Chem.* **45**, 493–519. https://doi.org/10.3906/kim-2101-19 (2021).
31. Yildiz, G., Bolton-Warberg, M. & Awaja, F. Graphene and graphene oxide for bio-sensing: general properties and the effects of graphene ripples. *Acta Biomater.* **131**, 62–79. https://doi.org/10.1016/j.actbio.2021.06.047 (2021).
32. Ullah, S. et al. Graphene transfer methods: A review, *Nano Research*, vol. 14, no. 11. pp. 3756–3772. https://doi.org/10.1007/s12274-021-3345-8 (2021).
33. Watson, A. B., Margetis, D. & Luskin, M. Mathematical aspects of the Kubo formula for electrical conductivity with dissipation. *Jpn J. Ind. Appl. Math.* **40** (3), 1765–1795. https://doi.org/10.1007/s13160-023-00613-7 (2023).
34. Organization, W. H. Tracking SARS-CoV-2 variants, *Who*. https://www.who.int/en/activities/tracking-SARS-Co (2021).
35. Patel, S. K. et al. SARS-CoV-2 detecting rapid metasurface-based sensor. *Diam. Relat. Mater.* **132**, 109644. https://doi.org/10.1016/j.diamond.2022.109644 (2023).
36. Wekalao, J., Baz, A. & Patel, S. K. Diamond & Related Materials Numerical analysis of an advanced infrared-based metasurface surface plasmon resonance sensor for COVID-19 detection. 149 (2024).
37. Patel, S. K. et al. Graphene-based H-shaped biosensor with high sensitivity and optimization using ML-based algorithm. *Alexandria Eng. J.* **68**, 15–28. https://doi.org/10.1016/j.aej.2023.01.002 (2023).
38. Upadhyay, A. et al. Biosensor performance signature enhancement with Silver-MXene-Graphene for brain tumor diagnosis through the employment of surface plasmon resonance. *Plasmon. No* https://doi.org/10.1007/s11468-024-02483-2 (2024).
39. Khodaie, A., Heidarzadeh, H. & Harzand, F. V. Development of an advanced multimode refractive index plasmonic optical sensor utilizing split ring resonators for brain cancer cell detection. *Sci. Rep.* **15** (1), 1–12. https://doi.org/10.1038/s41598-024-84761-x (2025).
40. Oudenani, A. & Sonne, A. A D – Shaped SPR – Based PCF Bio – sensor with a High Sensitivity for Wide Refractive Index Detection, *Plasmonics*. 2024. https://doi.org/10.1007/s11468-024-02689-4 (2019).
41. Lv, J. et al. Optical switching with high-Q Fano resonance of all-dielectric metasurface governed by bound States in the continuum. *Opt. Express* **32** (16), 28334. https://doi.org/10.1364/oe.530788 (2024).
42. Anushkannan, N. K., Wekalao, J., Patel, S. K. & Al-Zahrani, F. A. Design of encoded and tunable Graphene-Gold Metasurface-Based surface plasmon resonance sensors for glucose detection in the Terahertz regime. *Plasmon. No*. https://doi.org/10.1007/s11468-024-02452-9 (2024).
43. Liu, J. et al. High-Performance Gold-Nanowires-Coated PCF-SPR sensor for refractive index detection. *Plasmon. No*. https://doi.org/10.1007/s11468-024-02582-0 (2024).
44. Alshaikhli, Z. S. & Mahdi, M. T. Numerical analysis of high sensitivity refractive index sensor based on Quad-Core PCF-SPR. *Plasmon. No*. https://doi.org/10.1007/s11468-024-02651-4 (2024).
45. Cui, F., Yue, Y., Zhang, Y., Zhang, Z. & Zhou, H. S. Advancing biosensors with machine learning. *ACS Sens.* **5**, 3346–3364. https://doi.org/10.1021/acssensors.0c01424 (2020). no. 11.
46. Kokabi, M., Tahir, M. N., Singh, D. & Javanmard, M. Advancing healthcare: synergizing biosensors and machine learning for early Cancer diagnosis. *Biosensors* **13** (9). https://doi.org/10.3390/bios13090884 (2023).
47. Noor, J., Chaudhry, A. & Batool, S. Microfluidic technology, artificial intelligence, and biosensors as advanced technologies in Cancer screening: A review Article. *Cureus*. https://doi.org/10.7759/cureus.39634 (2023).
48. Zhang, P., Jia, Y. & Shang, Y. Research and application of XGBoost in imbalanced data. *Int. J. Distrib. Sens. Networks* **18** (6). https://doi.org/10.1177/15501329221106935 (2022).
49. Su, W. et al. An XGBoost-Based knowledge tracing model. *Int. J. Comput. Intell. Syst.* **16** (1). https://doi.org/10.1007/s44196-023-00192-y (2023).
50. Ben Jabeur, S., Mefteh-Wali, S. & Viviani, J. L. Forecasting gold price with the XGBoost algorithm and SHAP interaction values. *Ann. Oper. Res.* **334**, 1–3. https://doi.org/10.1007/s10479-021-04187-w (2024).

51. Budholiya, K., Shrivastava, S. K. & Sharma, V. An optimized XGBoost based diagnostic system for effective prediction of heart disease. *J. King Saud Univ. - Comput. Inf. Sci.* **34** (7), 4514–4523. https://doi.org/10.1016/j.jksuci.2020.10.013 (2022).
52. Patel, S. K. et al. Encoding and tuning of THz Metasurface-Based refractive index sensor with behavior prediction using XGBoost regressor. *IEEE Access.* **10**, 24797–24814. https://doi.org/10.1109/ACCESS.2022.3154386 (2022).

Acknowledgements

The authors acknowledge Princess Nourah bint Abdulrahman University Researchers Supporting Project number (PNURSP2025R400), Princess Nourah bint Abdulrahman University, Riyadh, Saudi Arabia.

Author contributions

"Conceptualization, HAE, JW; Methodology, AM, HEA, MRA, AH, WAZ; Software, AM, HEA, MRA, AH, WAZ; Validation, HAE, JW; Writing—original draft preparation, All authors; Formal Analysis, All authors; Writing— review and editing, All authors; All authors have read and agreed to the published version of the manuscript."

Funding

This study received funding through Researchers Supporting Project number (PNURSP2025R400), Princess Nourah bint Abdulrahman University, Riyadh, Saudi Arabia.

Declarations

Competing interests

The authors declare no competing interests.

Additional information

Correspondence and requests for materials should be addressed to J.W.